

PAPER • OPEN ACCESS

Finite element modeling and validation of a soft array of spatially coupled dielectric elastomer transducers

To cite this article: Sipontina Croce *et al* 2022 *Smart Mater. Struct.* **31** 084001

View the [article online](#) for updates and enhancements.

You may also like

- [Leakage current and induced electrical energy dissipation in nonlinear oscillation of dielectric elastomer actuators](#)

Junshi Zhang, Hualing Chen and Dichen Li

- [Electrical energy dissipation of dissipative dielectric elastomers](#)

Junshi Zhang

- [Halo approach to evaluate the stress distribution in 3D discrete element method simulation: validation and application to flax/bio based epoxy composite](#)

D Moukadiri, W Leclerc, K Khellil *et al.*



ECS Membership = Connection

ECS membership connects you to the electrochemical community:

- Facilitate your research and discovery through ECS meetings which convene scientists from around the world;
- Access professional support through your lifetime career;
- Open up mentorship opportunities across the stages of your career;
- Build relationships that nurture partnership, teamwork—and success!

Join ECS!

Visit electrochem.org/join



Finite element modeling and validation of a soft array of spatially coupled dielectric elastomer transducers

Sipontina Croce^{1,*} , Julian Neu¹ , Giacomo Moretti¹ , Jonas Hubertus² ,
Günter Schultes² and Gianluca Rizzello¹ 

¹ Department of Systems Engineering, Saarland University, Saarbrücken, Germany

² Department of Sensors and Thin Films, University of Applied Sciences of Saarland, Saarbrücken, Germany

E-mail: sipontina.croce@imsl.uni-saarland.de

Received 30 April 2022, revised 3 June 2022

Accepted for publication 14 June 2022

Published 29 June 2022



CrossMark

Abstract

Dielectric elastomer (DE) transducers are suitable candidates for the development of compliant mechatronic devices, such as wearable smart skins and soft robots. If many independently-controllable DEs are closely arranged in an array-like configuration, sharing a common elastomer membrane, novel types of cooperative and soft actuator/sensor systems can be obtained. The common elastic substrate, however, introduces strong electro-mechanical coupling effects among neighboring DEs, which highly influence the overall membrane system actuation and sensing characteristics. To effectively design soft cooperative systems based on DEs, these effects need to be systematically understood and modeled first. As a first step towards the development of soft cooperative DE systems, in this paper we present a finite element simulation approach for a 1-by-3 silicone array of DE units. After defining the system constitutive equations and the numerical assumptions, an extensive experimental campaign is conducted to calibrate and validate the model. The simulation results accurately predict the changes in force (actuation behavior) and capacitance (sensing behavior) of the different elements of the array, when their neighbors are subjected to different electro-mechanical loads. Quantitatively, the model reproduces the force and capacitance responses with an average fit higher than 93% and 92%, respectively. Finally, the validated model is used to perform parameter studies, aimed at highlighting how the array performance depends on a relevant set of design parameters, i.e. DE-DE spacing, DE-outer structure spacing, membrane pre-stretch, array scale, and electrode shape. The obtained results will provide important guidelines for the future design of cooperative actuator/sensor systems based on DE transducers.

Keywords: dielectric elastomer, array actuator, distributed actuator, spatial coupling, electro-mechanical coupling, finite element modeling, simulation

(Some figures may appear in colour only in the online journal)

* Author to whom any correspondence should be addressed.



Original content from this work may be used under the terms of the [Creative Commons Attribution 4.0 licence](https://creativecommons.org/licenses/by/4.0/). Any further distribution of this work must maintain attribution to the author(s) and the title of the work, journal citation and DOI.

1. Introduction

Nowadays, cooperative actuator systems have found application in a variety of fields, ranging from social communication (i.e. haptic devices [1, 2]) to safe human-machine collaboration [3]. On the one hand, large-scale cooperative systems have gained popularity thanks to their reliability, fault tolerance, and ability to perform tasks in a faster and more efficient way compared to stand-alone ones. Some examples include cooperative multi-robot systems for object transportation [4], cooperative manipulators [5], and cooperative robotic vehicles used especially in rescue missions [6]. On the other hand, concepts of distributed micro-motion systems have also been proposed [7]. In this case, simple movements of many coordinated microactuators (arranged in a serial or parallel layout) permit to perform more advanced tasks compared to the ones achieved by each individual microactuator. In this way, complex macroscopic behaviors naturally emerge from the cooperation of simple micro-scale systems, allowing the realization of innovative concepts, e.g. air-flow distributed [8] or silicon-based [9] actuator arrays micromanipulators, or microconveyors for sorting of small objects [10].

The successful development of such systems depends on the availability of actuator/sensor components capable of meeting scalability and energy-efficiency features. A critical point is represented by the design trade-offs between range of motion, strength, speed (i.e. actuation frequency), power consumption, control accuracy, system reliability, and robustness. As an example, thermal and magnetic actuators exhibit relatively large forces and displacements, but require high power input and cooling. Similarly, even though the silicon-based actuators mentioned above are suitable for miniaturization, they present drawbacks such as low energy efficiency (compressor) and camera-based closed-loop control (no self-sensing capabilities).

An alternative, unconventional, and less bulky way to enable cooperative devices is based on using dielectric elastomers (DEs) transducers. A DE consists of a thin elastomer film (acrylic, silicone) covered between compliant electrodes [11]. When a high voltage (HV) is applied to the electrodes, the resulting electrostatic forces squeeze the film, causing a reduction in thickness and a consequent expansion of the electrodes area, which can be used for actuation [12, 13]. A DE can also work as a sensor, since it is possible to infer information on the membrane deformation or the force acting on it by simply detecting changes in the transducer capacitance [14]. Actuation and sensing can be also executed simultaneously, thus realizing the so-called self-sensing, which permits to implement closed loop DE architectures with no need for external sensors [15–17]. Because of their lightweight, high strain range (above 100%) [18], low cost, high energy efficiency, and scalability, DEs can be effectively used in applications such as fluidic systems [19], haptic devices [20, 21], valves [22], loudspeakers [23–25], pumps [26], artificial muscles [27], medical systems [11, 28], and wearable stretch sensors [29, 30], to mention some prototypes presented in the literature. The high scalability, energy efficiency, and dual actuator/sensor

behavior (self-sensing) of DEs have made them also popular for the development of small-scale cooperative systems. In contrast to alternative cooperative devices based on microvalves and MEMS actuator technologies, the intrinsic flexibility and large deformation of DEs enables the development of new applications, e.g. intelligent wearables, smart skins, and soft robots. By coupling cooperative DE systems with distributed self-sensing control algorithms, complex tasks can be achieved within a fully integrated soft system. Despite the great potential of DE technology for such application fields, only few examples of cooperative small-scale actuator systems have been presented in the literature so far. These include cooperative DE actuators for tactile display applications [31], haptic communication based on a wearable actuator array [32], and cooperative hydraulically amplified DE actuator (DEA) cell arrays for feedback devices [33]. In all the examples above, cooperation is achieved via software, since all DE elements are mechanically and electrically decoupled. This solution has the advantage of simplifying the system design and control, but it comes with the drawback of requiring additional rigid components (e.g. spacers, compressors for pneumatic biasing), which unavoidably affect the overall system flexibility and weight. In addition, by keeping the single actuation unit mechanically independent, those system lose some features in terms of embedded intelligence, e.g. the possibility of implementing self-sensing based cooperative controls.

A shift in paradigm can be obtained by developing fully-polymeric cooperative systems, in which several DE elements share a common elastic layer in an array configuration. In this way, flexibility of the overall system can be maintained while introducing cooperative features at hardware level (i.e. spatially coupled electro-mechanical interactions among nearby DE elements). To understand how to design and optimize the geometry, the layout, and the number of active DE elements for such kind of applications, numerical simulation tools play a key role. Among them, the finite element (FE) method is among the most promising ones. Due to their ability to perform accurate structural simulations and address coupled problems involving large deformations, FE methods have been extensively used to analyze DE systems, see, e.g., [34–38]. The vast majority of the FE models presented so far, however, focused on simple (i.e. stand-alone) DE systems. In principle, FE simulations appear as an ideal tool to analyze and optimize cooperative DE devices as well, which are significantly more complex than their stand-alone counterparts. By means of FE simulations, one can systematically study how the system parameters (i.e. geometry, pre-load, electrode shape and location) affect the system performance as well as the spatial coupling among neighbor DEs, and use this information to embed smart cooperative functionalities into the design. To date, however, the investigation of cooperative DE systems based on FE analysis has only received little attention in the literature [39].

As an initial step towards the realization of a flexible and cooperative DE system, in this work we present and validate for the first time a FE model of a soft array of DE transducers. The system consists of a silicone membrane with

compliant carbon-based electrode patches on both faces, forming a 1-by-3 array layout. This concept, initially presented in [40], can be combined with a layer of soft biasing systems (e.g. the bi-stable dome proposed in [41]) that provide the DE units with an off-plane pre-load. This allows the units to generate a linear actuation in response to a voltage, and potentially makes it possible to use the array as a cooperative actuator/sensor system capable of large strokes and intrinsic compliance. Possible applications based on the presented DE array layout include soft conveyors (in which an object is transported in between two target points passing through a series of DE units), or conformable multi-unit tactile displays (e.g. Braille displays). Due to spatial coupling effects caused by the continuous elastic substrate, the activation of one DE in the array influences the actuation and sensing properties of its neighbor elements [42]. To understand how the system parameters affect the resulting coupled performance, and to achieve optimal system designs which allow effective implementation of cooperative actuation/sensing paradigms, a FE model is proposed here. Large deformations, electro-mechanical coupling, and geometric nonlinearities are accounted for by means of a physics-based membrane formulation of the FE problem. The model is calibrated and validated based on a large number of experimental data, which aim at characterizing how spatial coupling affects the force (actuation) and capacitance (sensing) responses of the different elements in the array, when subject to different combinations of loading conditions. An overall good accuracy is achieved, with force and capacitance fit on the order of 93% and 92%, respectively. The validated model is finally used to perform a parameter study, which allows us to gain an initial understanding on how the intrinsic coupling can be affected by modifying the array design parameters (e.g. geometry, pre-stretch, scale, electrode shape). The obtained results will provide fundamental insights for the future optimization and control of cooperative DE systems. We also point out that the considered paper extends the preliminary results presented in [39], by including: a more detailed formalization and description of the FE model; a detailed discussion on FE model implementation issues; the inclusion of the DE capacitive response in both model and experiments; a more extensive experimental campaign; an extensive parameter study based on the calibrated model.

The remainder of this paper is organized as follows. In section 2, the operating principle of DE actuators and sensors is presented. The 1-by-3 array concept is then described in section 3, followed by the FE model formulation in section 4. Model calibration and validation then shown in section 5. A model-based parameter study is finally conducted in section 6, followed by concluding remarks in section 7.

2. DE working principle

The working principle of DE transducers is briefly described in this section, focusing on both the actuator and sensor working modes. As previously stated, a DE is a flexible capacitor consisting of a polymer membrane covered by two patches of

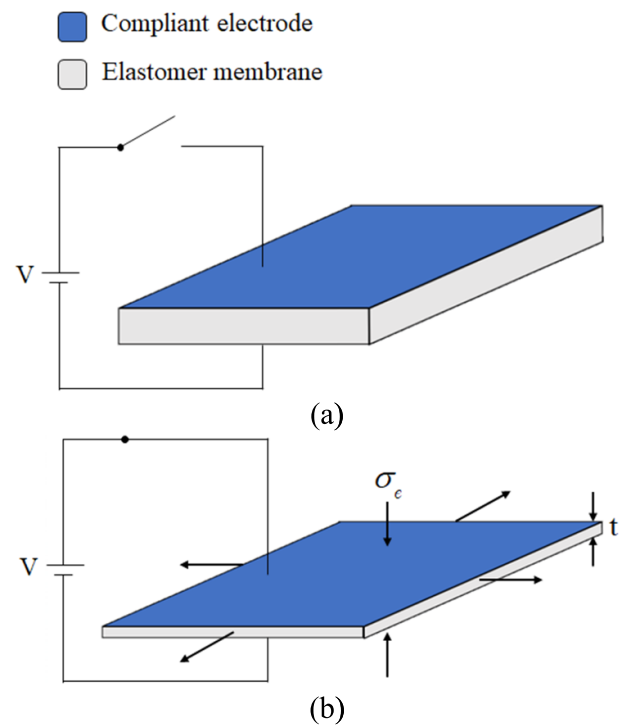


Figure 1. Operating principle of a DEA: configuration without (a) and with electrical activation (b). Due to the Maxwell stress, the membrane thickness reduces while its area expands.

compliant electrodes. The polymer film is generally made of acrylic or silicone material [43, 44], while carbon or silicone-carbon mixtures represent common material choices for the compliant electrodes [45]. More recently, novel approaches based sputtered thin metal films (thickness in the nanometer scale) have been proposed as alternative solution for highly stretchable and conductive electrodes, which appear especially suitable for energy efficient and miniaturized applications [46].

The basic working mechanism of a DEA is described in the following, and schematically shown in figure 1. The application of a HV between the compliant electrodes (typically in the range 1–10 kV for a film thicknesses within 20–100 μm [14]) results in an electrostatic compressive force which squeezes the membrane, causing it to reduce in thickness and expand in area (figure 1(b)). The resulting voltage-induced stress, referred to as Maxwell stress, is denoted σ_e and is quantified as follows [12]:

$$\sigma_e = -\epsilon_0 \epsilon_r \left(\frac{V}{t} \right)^2, \quad (1)$$

where ϵ_0 is the vacuum permittivity, ϵ_r is the DE relative permittivity, V is the applied voltage, and t is the thickness of the film (note that the ratio V/t represents the average electric field in the material). In order to achieve a usable actuation stroke, a DE membrane is generally coupled with a biasing element (e.g. a mass or a linear spring). In this case, the electrical activation causes a softening of the DE which, in turn, allows the

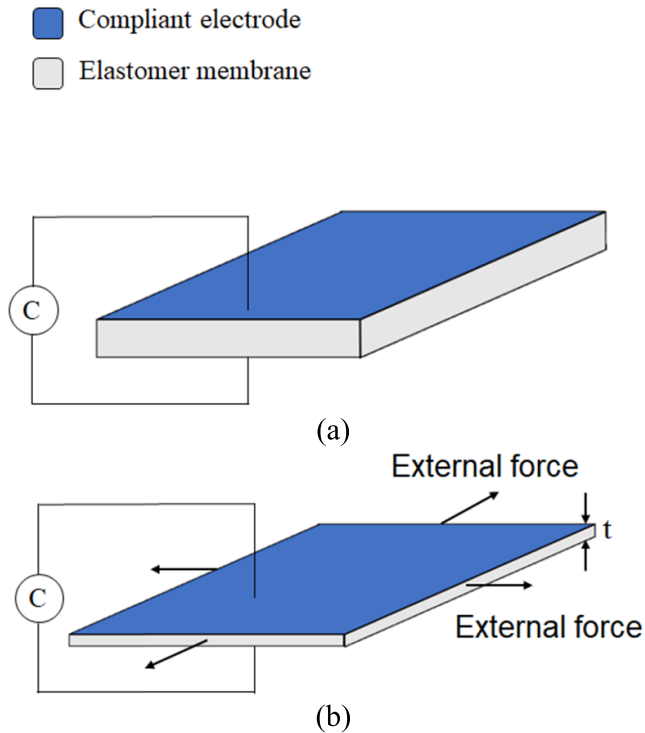


Figure 2. Operating principle of a DES: configuration without (a) and with external force applied (b). The external force causes an area expansion and a thickness reduction, resulting in a capacitance increase.

biasing system to displace it further, until a new equilibrium state is reached. The resulting DEA stroke is defined as the difference between the elastomer deformations when the voltage is on and off, respectively. In the literature, a number of studies have shown how the use of negative-stiffness biasing elements (NBS) can allow to significantly increase the actuation performance, compared to conventional biasing springs (LBS) or masses. In DEA applications, those negative-stiffness elements are generally obtained via pre-compressed steel beams [47], attracting permanent magnets [48], or buckling silicone domes [41], the latter being particularly suited for achieving a fully-polymeric design.

Other than being used for actuators, DEs also appear as highly suitable for the realization of sensors. The operating principle of a DE sensor (DES) can be easily understood by approximating the capacitance of a DE membrane, denoted with C , with that of a parallel-plate capacitor [14]:

$$C = \epsilon_0 \epsilon_r \frac{A}{t}, \quad (2)$$

where A is the electrode area, while all the other parameters have been defined previously. As shown in figure 2, if an external in-plane force is applied to the DE, it causes A to increase and t to simultaneously decrease (since the volume $A \cdot t$ remains constant because the elastomeric material is incompressible). Both effects cause C to increase (cf (2)). This way, a monotonic relationship can be established between the DE capacitance and its state of deformation. Both DEA and DES

working modes can be eventually executed at the same time, obtaining a self-sensing device [15, 16].

3. Soft DE array

This section describes a prototype of a 1-by-3 array of circular DEs, which is here used as an archetypal layout of soft and cooperative DE system.

3.1. Array geometry description

The general layout of the DE array experimental prototype used as reference for this study is shown in figure 3. The device is made of a bi-axially pre-stretched rectangular membrane of silicone material (Wacker Elastosil 2030, 50 μm thickness [49]), with three carbon-based circular electrodes screen-printed on both surfaces. The main geometric parameters of the system are also reported in figure 3. The electrode patches define three independent active parts on the DE membrane, which can be deformed out-of-plane (e.g. via a biasing mechanism) and electrically actuated via a HV (thus resulting in an out-of-plane stroke). Each electrode region has a circular shape with diameter $D = 20$ mm. The minimum distance between electrode patches and between the electrodes and the external border are denoted d and b respectively, with $d = b = 15$ mm. Finally, radius $r = 2.5$ mm identifies a circular area, within the electrode patches, on which external forces are applied (in the experiments presented here, by means of an indenter, as discussed in [42]).

The layout shown in figure 3 can be used to develop actuator systems by coupling the DE with elastic biasing elements (as shown in figure 4 and further discussed in section 3.2), that provide the single units with an out of plane pre-load. This way, the single units have a behavior qualitatively similar to a so-called cone DEA [16], and can separately produce off-plane linear strokes when subject to a voltage. If no rigid frames are applied in between the different units so as to render their response independent, the equilibrium shape of the array and the resulting electro-mechanical response are complex functions of the deformation of the single units.

The main reason for the choice of this layout for the aim of the present analysis is its simplicity and fully-polymeric structure. On the one hand, it enables a clear characterization of spatial coupling electro-mechanical effects among neighbor DEs. On the other hand, its geometry provides a simple proof-of-concept for the validation of the developed FE model. Although this layout with only three active units represent a first archetypal implementation of a DE array, more complicated concepts might be built upon the same principle, using a larger number of in-line elements or complex multi-row multi-column configurations.

3.2. Spatially coupled electro-mechanical effects

With the aim of pointing out the importance of investigating and characterizing coupling effects in DE arrays, in this section we present an example of a DE system based on the layout discussed in section 3.1, and discuss the implications of

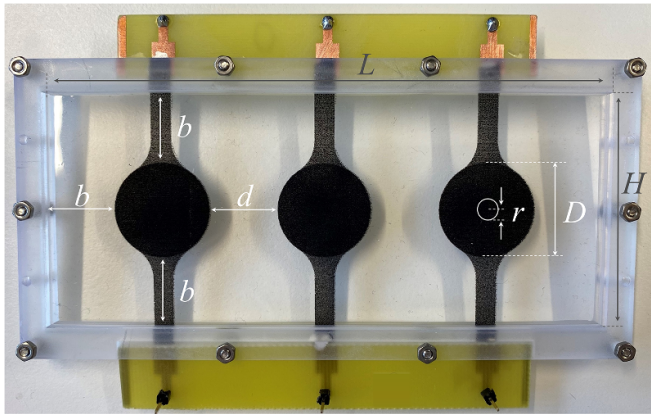


Figure 3. Picture of the 1-by-3 DE array prototype, also showing the main geometric parameters.

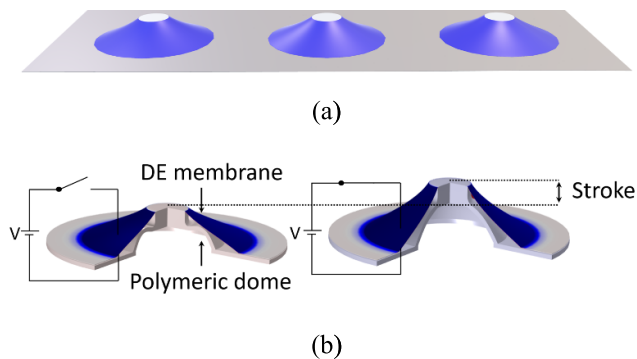


Figure 4. DEA array layout. (a) 1-by-3 array 3D rendering; (b) cross-sectional view of the DE membrane coupled with a polymeric biasing dome. On the left-hand side, the actuator is in the undeformed configuration. On the right-hand side, upon voltage application, the actuator reaches a different equilibrium position. The out-of-plane displacement of the DEA results in a linear actuation stroke.

interactions among neighbor elements on the system design. For this purpose, we make reference to the system shown in figure 4. In this layout, each DE element in the array is pre-loaded with a bi-stable silicone dome. As discussed in [41] as well as in section 2, if properly matched to the characteristics of the DE membranes, those domes ensure a large actuation stroke while keeping an overall flexible design.

While matching a biasing system to the elastomer force-displacement curves is generally simple for individual DEAs, this process presents several challenges in case of the considered array. In this case, indeed, the proximity among the different DEs causes strong electro-mechanical interactions, because the deformations and electric loads applied on one of the elements affect the stress and electric field distribution on its neighbors. More explicitly, given the same displacement and voltage applied to a DE within the array, its force and capacitance responses will differ depending on the loading state of the neighboring elements. This effect makes the actuation and sensing characteristics of each DE strongly coupled to the state of their neighbors. If properly exploited, this coupling might be used to embed cooperative features within the array,

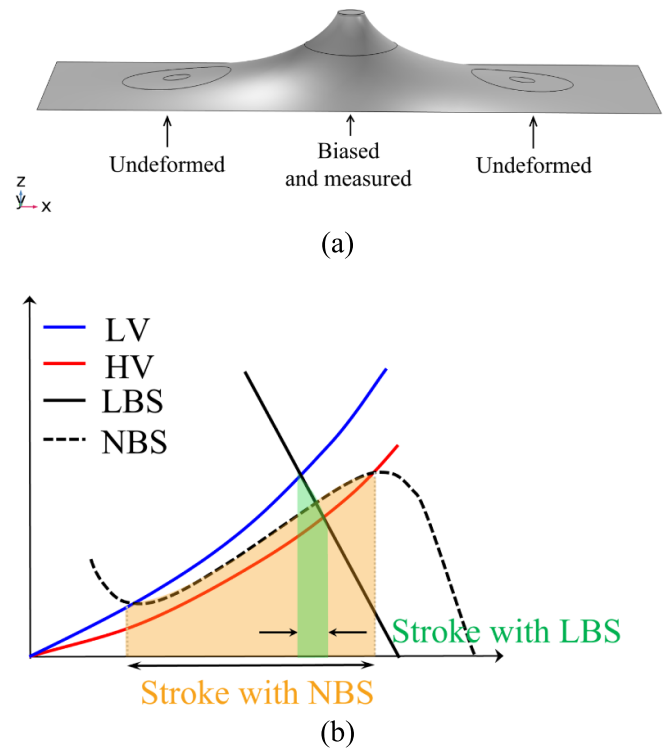


Figure 5. Nominal DE characterization curves: (a) deformation of the second DE membrane starting from the initial undeformed array configuration; (b) characteristic curves of the second DE membrane, showing the effects of different types of biasing systems.

e.g. the DEs can detect when their neighbors are moving by monitoring their own capacitance, and use this information to propagate a wave pattern. Conversely, if not properly accounted for in the design stage, the coupling could also lead to detrimental effects, which may severely affect the overall system performance.

For a better understanding of the phenomenon, we consider the examples shown in figures 5 and 6. Those figures depict the qualitative force-displacement curves of the central DE of the array in two testing conditions, namely when its neighbors are undeflected (figure 5), and when the neighbors are pre-deflected out of plane by a constant amount (figure 6), respectively. In both cases, solid lines correspond to the out-of-plane force-displacement characteristics of the second DE in the array, obtained for low (blue) and high (red) applied voltage, respectively. Two distinct types of biasing elements are considered, namely a LBS (solid black line) and a NBS (dashed black line). As it can be observed from figure 5(b), if the NBS curve is properly matched to the DE ones, it allows for a much higher stroke compared to the LBS. In case the neighbors are deflected, however, the curves of the second DE undergo a change (compare the dotted and solid lines in figure 6(b)). Therefore, if we use the NBS optimized for the nominal case (on a single DE unit) while allowing the neighbors to deflect, the resulting DE stroke is drastically reduced. This issue is especially critical when a NBS is used as biasing element. In fact, the optimal design of a NBS is usually performed graphically, based on DE force-displacement

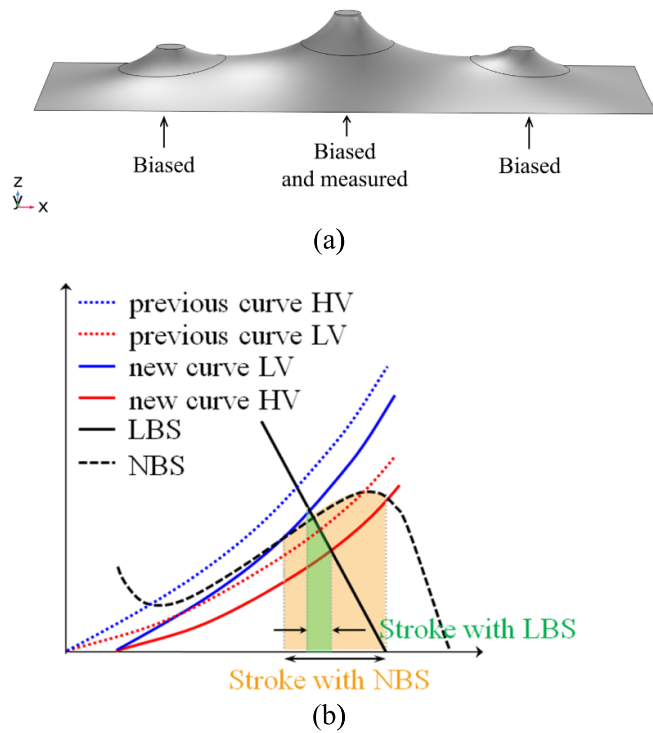


Figure 6. Perturbed DE characterization curves: (a) deformation of the second DE membrane starting from an initial condition with pre-deflected neighbors; (b) the characteristic curves of the same membrane undergo a change compared to the nominal case (dotted lines). In this case, coupling the second DE membrane with same bias element from the previous case causes a sensible decrease in stroke.

characteristics measured in nominal conditions, and is generally highly sensitive to the shape of those curves [41]. We conclude that, for a DE array, the design of a suitable biasing system capable of guaranteeing large strokes for each actuator must be performed in a monolithic way, explicitly keeping into account the interactions among neighbor elements. Similar considerations can be made concerning the sensing behavior, since the capacitance of a DE in the array depends not only on its deformation state, but also on the displacement of its close neighbors. Therefore, a capacitive sensing strategy which ignores the intrinsic coupling effects is destined to fail.

4. FE model and implementation

In this section, a FE model is developed for the 1-by-3 DE array in figure 7. The model considers the out-of-plane displacement and the voltage of each DE in the array as independent inputs, and predicts their resulting out-of-plane force and capacitance as outputs. For the aim of the present analysis, we set our attention on the static response of the array and neglect the contribution of dynamic effects (e.g. inertial loads or viscoelastic effects). The validation presented in section 5 shows that, even with this simplified setting, the model is able to capture the main coupling effects among the different array elements, which arise as a consequence of mutually-induced deformations among the units.

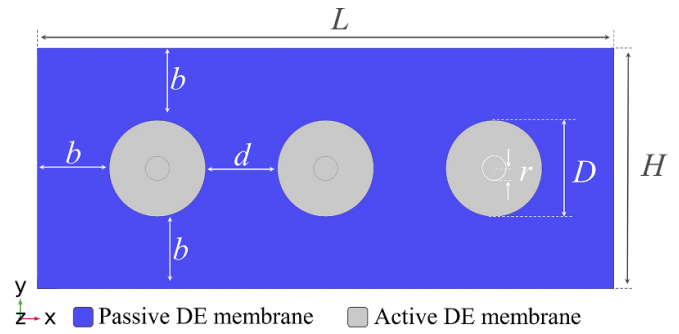


Figure 7. Three-dimensional rendering of the 1-by-3 array of DEs, showing the meaning of the nomenclature for the geometric parameters.

4.1. Continuum model

In this subsection, details related to the model governing equations and boundary conditions are discussed.

4.1.1. Assumptions and equilibrium equations. The DE membrane is treated as a continuum elastic body with coupled electro-elastic response, subject to large deformations [50]. The same assumptions as in [51] are made. The DE is mechanically modeled as an initially-flat thin membrane element with negligible bending stiffness. Stresses/stretchches are assumed uniform along the thickness, and no stress acts in the thickness direction. The electrically active portions of the membrane (i.e. the areas covered by electrodes) are electrically modeled as ideal dielectrics subject to an electric field perpendicular to the membrane surface, and the contribution of the electrostatic stresses (Maxwell stress) in the presence of an applied electric field is accounted for resorting to established continuum electro-elastic formulations [52]. We denote X - Y - Z a material frame describing the coordinates of the points on the undeformed membrane, such that the membrane undeformed surface lies on the X - Y plane and the thickness is aligned with the Z direction (see figure 7). The thickness direction is a principal deformation direction for all the membrane points, with the other principal directions lying on the membrane surface (and generally varying throughout the different membrane points).

In static condition, neglecting the effect of distributed body loads (e.g. gravity, which are assumed negligible compared to the electro-elastic contributions), inertia and viscous effects, the equilibrium of the membrane is described by the following equation:

$$\text{DIV}(\mathbf{P}) = \mathbf{0} \quad (3)$$

where \mathbf{P} is the first Piola-Kirchoff tensor, whose elements represent the nominal stresses on the membrane, and operator DIV is the divergence calculated with respect to a material frame (i.e. with respect to the coordinates of the material points in the undeformed configuration). Because of the thin membrane assumption, $P_{i,3} = 0$ for $i = 1, 2, 3$ with $i = 3$ denoting the Z direction (whereas the elements $P_{3,i}$ in general might be different from 0). Stress tensor \mathbf{P} is related to the membrane

stretches and the electric field applied on the DE via a suitably defined constitutive model (see section 4.1.2).

4.1.2. Constitutive equations. In terms of the constitutive mechanical model, the membrane is treated as an incompressible hyperelastic solid [50], in which the relationship between the stress tensor \mathbf{P} and the stretches/applied electrical load is formulated in terms of a free-energy function.

The active DE areas (grey regions in figure 7) are described via a free-energy density function in the form $\Psi = \Psi_M + \Psi_E$. The first term of Ψ describes the membrane elastic energy by means of a Yeoh constitutive model [50], while the second one represents an added electrostatic co-energy potential, which is used to render the contribution of electrostatic stresses [51]. The mechanical and electrostatic contributions to the free-energy density are formulated as follows:

$$\Psi_M = \sum_{i=1}^3 c_{i0} (\lambda_1^2 + \lambda_2^2 + \lambda_3^2 - 3)^i + p(J - 1), \quad (4)$$

$$\Psi_E = -0.5\varepsilon_0\varepsilon_r J \left(\frac{V}{\lambda_3 t_0} \right)^2, \quad (5)$$

where: c_{i0} , $i = 1, 2, 3$ are constitutive parameters describing the Yeoh model (here assumed constant and independent of the ambient conditions, at a first order); λ_1 , λ_2 , λ_3 represent the principal stretches, in particular λ_1 and λ_2 are the principal stretches in the in-plane principal directions, whereas λ_3 is the stretch in the thickness direction; p is a Lagrange multiplier that accounts for the material incompressibility constraint; $J = \lambda_1\lambda_2\lambda_3$ represents the volume ratio (i.e. the determinant of the deformation gradient); t_0 represents the initial (unstretched) membrane thickness; V represents the applied voltage (hence, V/t_0 represents the nominal electric field on the dielectric).

The passive areas of the array (blue regions in figure 7) are described via a free-energy density function which only includes the elastic contribution, i.e. $\Psi = \Psi_M$ (where Ψ_M is modeled with the same Yeoh free-energy function used for the active part). No electrostatic contribution is accounted for in the passive regions, i.e. the effects of fringing electric fields due to the neighbor active regions is neglected.

The elements of the Piola-Kirchoff stress tensors (used in (3)) can be expressed in terms of the strain energy function as follows:

$$\mathbf{P} = \frac{\partial \Psi}{\partial \mathbf{F}} \quad (6)$$

where \mathbf{F} indicates the gradient of the deformation.

Finally, the capacitance of a given DE element is computed as follows:

$$C_k = \int_{A_{0,k}} \frac{\varepsilon_0\varepsilon_r\lambda_1\lambda_2}{t_0\lambda_3} dA_{0,k}, \quad (7)$$

where $A_{0,k}$ ($k = 1,2,3$) represents the area of the k th undeformed DE patch.

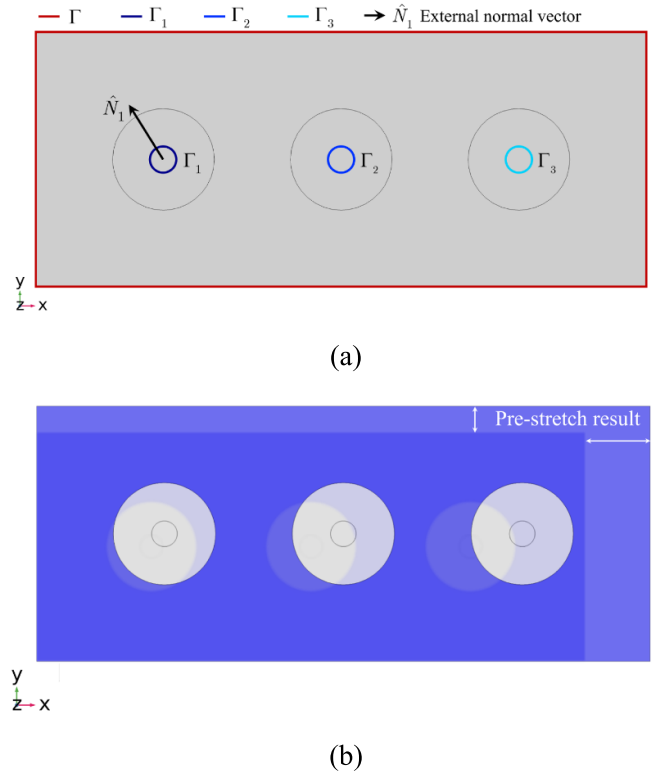


Figure 8. FE implementation of the 1-by-3 DE array: (a) boundary conditions applied; (b) final resulting array including pre-stretch.

4.1.3. Boundary conditions. The control inputs, boundary conditions, and computed outputs emulate the real constraints present on the experimental prototype. In particular, the model makes use of prescribed displacements and voltage as the inputs, chosen independently for each DE unit.

Prescribed displacements u , v , and w in the X , Y and Z directions respectively are applied on the external perimeter Γ of the membrane, so as to account for an equi-biaxial pre-stretch λ_p applied during the manufacturing process, before the membrane is rigidly clamped to the external rigid frames (figure 8(a))

$$\begin{cases} u = (\lambda_p - 1)X \\ v = (\lambda_p - 1)Y \\ w = 0 \end{cases}, \quad (X, Y, Z)^T \in \Gamma. \quad (8)$$

The in-plane pre-stretch deformation resulting from the application of boundary condition (8) is represented in figures 8(a) and (b).

To control the DEs out-of-plane deformation, a prescribed displacement boundary condition is applied on circular areas (with radius r) at the center of one or more of the active annular elements:

$$\begin{cases} u = (\lambda_p - 1)X \\ v = (\lambda_p - 1)Y \\ w = d_k \end{cases}, \quad (X, Y, Z)^T \in \Gamma_k \quad (9)$$

where d_k represents the axial displacement applied of the k -th unit (with $k = 1, 2, 3$), which is subject to a prescribed displacement. This boundary condition is used to emulate the behavior of a rigid indenter of radius r that, driven by a linear motor, pushes the membrane out-of-plane during the characterization tests (cf figure 3). The reaction-force F_k in the Z-axis direction from the same circular surface can be calculated from the membrane stresses as follows:

$$F_k = t_0 \int_{\Gamma_k} \mathbf{P} \hat{\mathbf{N}}_k \, d\Gamma_k \quad (10)$$

where the integral in (10) is calculated along the undeformed inner perimeter of the k th annular patch, and $\hat{\mathbf{N}}_k$ represents the nominal outer normal unit vector of frontier Γ_k .

4.2. FE implementation

The model described in section 4.1 is numerically tackled by means of a FE formulation, implemented in COMSOL Multiphysics®. The 3D rendering of the implemented model (showing the membrane in the reference undeformed configuration) is reported in figure 7. The developed FE implementation makes use of in-built membrane elements from the nonlinear structural module. The built-in form of the Yeoh hyperelastic free-energy is modified in the active portions of the membrane via custom-defined expressions, so as to include the contribution of the applied voltage (equation (5), where V is a user-defined input). The domain is discretized using free triangular meshes (see section 4.2.2).

4.2.1. Comparison with a fully-coupled three-dimensional formulation. Because of the extremely high surface-to-thickness ratio of the considered membrane (on the order of 10^5 m), the formulation presented in section 4.1 treats the DE as a thin membrane element, assuming that the electric field distribution is the same as in a parallel plate capacitor, and neglecting fringe electric fields (the latter assumption is also motivated by our previous studies in [53], in which we showed that fringing fields have a negligible impact on the overall array output). In this section, we validate these assumptions by comparing the predictions of the presented formulation with those of a fully-coupled three-dimensional formulation. The latter is implemented following the approach presented by Verthey *et al* [54]. The 3D model is implemented via the built-in Nonlinear Structural and Electrostatic modules in COMSOL Multiphysics®, treating the membrane as a thin parallelepiped (figure 9(a)) with prescribed electric potential on the outer surfaces of the active portions, and explicitly solving for the stress and the electric field distributions over the entire membrane volume. The electro-static coupling is implemented using the approach described in [54], i.e. by introducing a dependency of the free-energy function on the spatial components of the electric field. Compared to the membrane formulation presented in section 4.1, the fully-coupled 3D implementation requires a much larger number of mesh elements (since the domain is fully discretized also in the thickness direction), and brings

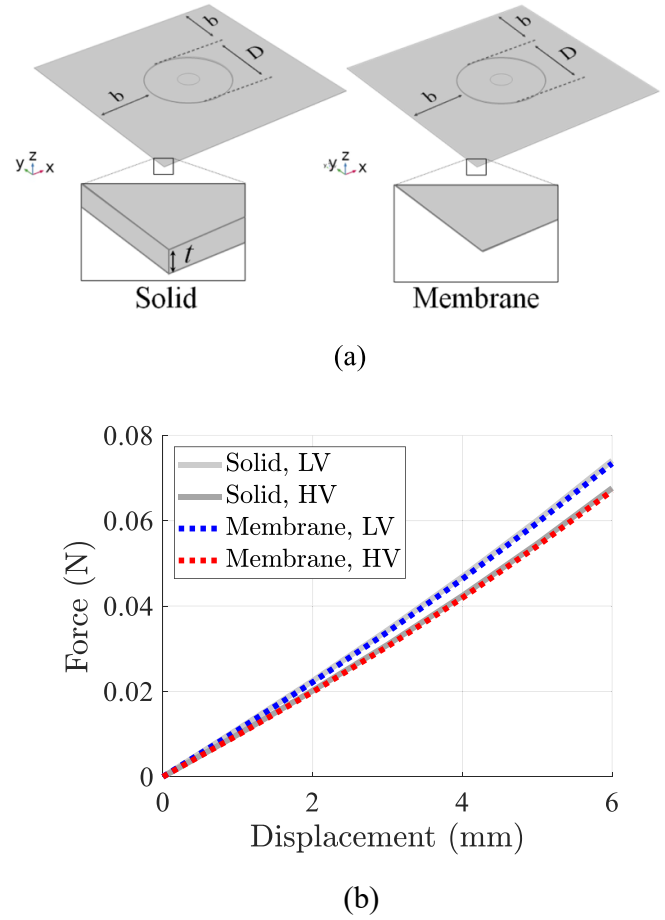
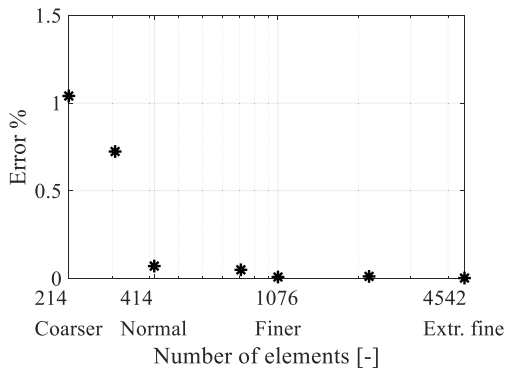


Figure 9. Comparison between 3D and membrane physical interfaces in terms of the force-displacement response up to 6 mm: (a) solid and membrane physical interfaces solutions, highlighting the difference over the two models is the thickness built in addition in the full 3D one; (b) force-displacement curves resulting from both the full 3D physical interface and the membrane solutions.

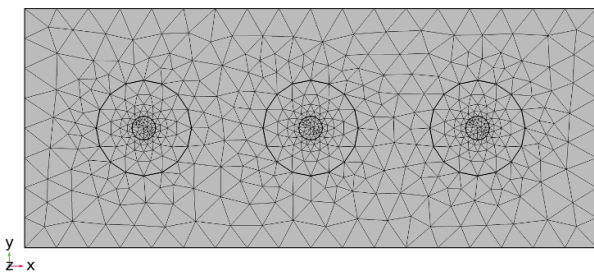
along a significantly larger computational burden (since also the electrostatics are explicitly solved for).

For the sake of this analysis, we consider a single DE membrane with the dimension defined in figure 9(a) (the same numerical values as discussed in section 3.1 are used), subject to a pre-stretch $\lambda_p = 1.10$. For the simulations, the material parameters are chosen as in our previous work [53], while the boundary conditions are set equivalently to section 4.1.3. The membrane deformation is applied on the central portion of the active area as a prescribed displacement (9), and the reaction-force along the Z-axis is evaluated accordingly. The two models (3D and membrane) are compared in terms of the force-stroke response of the membrane at $V = 0$ V and $V = 2730$ V (figure 9(b)). The 3D and membrane models turn out to be equivalent, since they produce the same characteristic curves shown in figure 9(b). The membrane model shows an average error of less than 1% compared to the 3D one, while requiring only 30% of its simulation time.

Based on this outcome, we conclude that the membrane element represents a suitable choice to perform FE simulation studies on the DEs array, and it presents significantly lower



(a)



(b)

Figure 10. Mesh convergence study: (a) quantification of the average relative percentage error resulting among the actual mechanical characteristic (obtained with a given mesh), and those resulting from the previously set mesh; (b) 2D FE, with a *finer* mesh defined.

computational burden than the three-dimensional model, without causing significant loss in prediction performance.

4.2.2. Mesh refinement study. The computational accuracy in the FE model depends on the distribution of dependent variables in the geometry. For this reason, a mesh is generated to induce a discretization of the model. The greater the number of mesh elements, the more accurate the results will be, with the drawback of increasing the number of operations and consequently the computation time. In this section, we perform a convergence analysis aimed at identifying a suitable dimension for the FE model mesh. To this end, we use different standard mesh sizes available in COMSOL, each one resulting in a different number of elements in the model:

- *Coarser*—214 elements;
- *Normal*—414 elements;
- *Finer*—1076 elements;
- *Extremely fine*—4542 elements.

An unstructured free triangular mesh is initially set. Next, the model is run on a set of progressively finer meshes, and the results for the different cases are compared. The standard in-built options for mesh size are used for this analysis (ranging from the *coarser* to the *extremely finer* mesh). For the convergence analysis, we considered the same material properties as in section 4.2.1, and simulated a scenario in which

the 3-by-1 array shown in figure 7 has no voltage applied on the active patches ($V = 0$ for all DEs), and an axial displacement of 15 mm is applied on the central unit (whereas the outer units are left unconstrained). The average relative percentage error, computed by comparing the force-displacement curves of the central DE for two consecutive mesh choices, is reported in figure 10(a). A progressive reduction of the percentage error occurs as the mesh is gradually refined, indicating that the solutions reach convergence. In fact, even with the *coarser* mesh, the relative error is on the order of 1%. This suggests a possible use of a relative coarse mesh as a means to reduce the computational cost for the overall model, without a significant loss of information on the system behavior. For this work, we selected the *finer* mesh type for the entire structure, as it represents an acceptable trade-off between simulation time and accuracy. The 3D rendering of the selected mesh is shown in figure 10(b).

5. Experimental results

To evaluate the accuracy of the presented FE model, a calibration and validation campaign is presented in this section. These are conducted on a large set of experimental data, which highlighting the mechanical coupling among DEs in a variety of loading conditions. In this way, the effectiveness of the model can be evaluated in a large variety of interaction scenarios.

5.1. Experimental characterization

An experimental setup was assembled to perform several experiments, which highlight the mechanical coupling among DEs in a variety of loading conditions. The setup, shown in figure 11, allows measuring the force (in the presence of a LV or HV) and capacitance (when no voltage is applied) of a target DE unit, while at the same time applying a static pre-loading to the remaining units. The static pre-loading of the non-measured DEs is applied by means of an indenter module, while the force-displacement response of the target DE unit is measured through a separate indenter connected with a linear motor (Aerotech Inc., ANT25-LA) and a load cell (ME-Meßsysteme GmbH, KD40s). Capacitance measurements, instead, are acquired via an LCR-meter (Rohde & Schwarz GmbH & Co. KG, HM8118).

A large set of experimental data is created by selecting different combinations of the following array parameters:

- Static pre-deflection applied to neighboring (non-measured) DE elements (before taking force-displacement measurements of the membrane of interest): 0 mm, 4 mm, 6 mm, 8 mm;
- Biaxial pre-stretch of the DE array: 10%, 20% of the array height and length (two separate arrays with a different pre-stretch are manufactured for this purpose);
- Voltage applied on the DE: a low voltage (LV) level of 0 V and a constant HV level, the latter computed in such a way to achieve a safe electric field value of $80 \text{ V } \mu\text{m}^{-1}$ when reaching the maximum displacement [49].

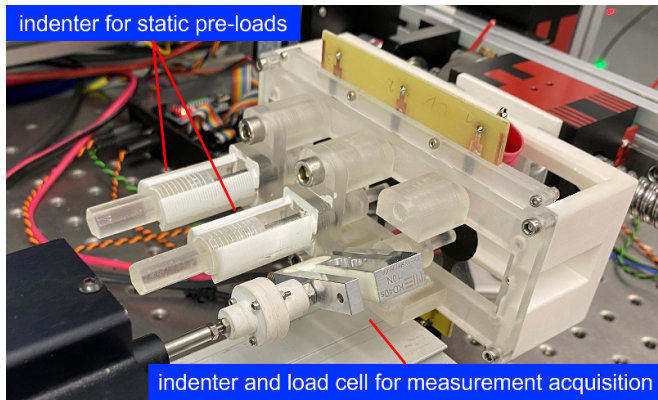


Figure 11. Picture of the experimental setup use to characterize the 1-by-3 DE array.

It shall be pointed out that the chosen combinations of pre-loads do not necessarily represent operating configurations for the final DEAs array, but they are relevant for highlighting interactions among neighbors and developing optimal biasing system design algorithms. For each considered combination of pre-deflection, biaxial pre-stretch, and applied voltage, characterization tests are conducted by deforming the DEs off-plane up to 15 mm. Under this condition, the applied HV value equals 2730 V for the 10% pre-stretch, and 2300 V for the 20% pre-stretch, respectively. The tests are conducted in quasi-static conditions, so as to eliminate the DE viscoelastic hysteresis, whose effects are not included in the developed model. For additional details on how the experimental measurements are carried out, the reader may refer to [42].

5.2. Model calibration and validation

Most of the model parameters are known in advance, i.e. those related to the array geometry and the material permittivity and pre-stretch (table 1). The only parameters that require a calibration are those describing the hyperelastic Yeoh model, namely c_{10} , c_{20} , and c_{30} in (4). Datasheet information about the elastic response of the material is indeed provided only for the case of uniaxial strains, and is not sufficiently descriptive of the complex multi-axial deformation state considered in this work. Moreover, because the hyperelastic parameters used here describe, in an average manner, the response of the composite electrode-dielectric membrane structure, they are prone to a certain degree of variability among different DE samples' batches. Such parameters are calibrated *a-priori* using a part of the experimental dataset, namely the curves corresponding to the array with a 10% pre-stretch and neighbors pre-deflected by 4 mm and 6 mm.

The optimization module in COMSOL is used for identifying the structure parameter, by choosing the Nelder-Mead optimization method. Identification is performed by finding the parameter values that minimize a cost function expressing the deviation between the simulated and the experimental force-displacement characteristics. The optimal values of the calibrated parameters are reported in table 1.

Table 1. Known and identified model parameters.

Coefficient	Symbol	Value	Unit
Array geometry—known			
Total array length	L	200	(mm)
Total array width	H	50	(mm)
Electrode diameter	D	20	(mm)
Electrode spacing	d	15	(mm)
Electrode-outer edge spacing	b	15	(mm)
Biaxial pre-stretch	λ_p	1.10, 1.20	(—)
Array thickness	t_0	50	(μm)
Material coefficients—known			
Vacuum permittivity	ϵ_0	8.85	(pF/m)
DE relative permittivity	ϵ_r	2.8	(—)
Material coefficients—identified			
Yeoh model parameters	c_{10}	0.18	(MPa)
	c_{20}	10.84	(kPa)
	c_{30}	-0.11	(kPa)

As a first validation step, the calibrated model is compared with experimental capacitance measurements. To this end, two separate experiments are considered, both of them performed under LV conditions. In the former test, the second DE is deformed up to 15 mm while its capacitance deviation from the initial value is measured, and its neighboring elements are not subject to any pre-deflection. In this case, a large capacitive change is observed. In the second experiment, we always measure the capacitance deviation of the second DE, but this time we only deflect the first DE out of plane up to 15 mm. Interestingly, the deformation on the first DE causes a small, yet measurable change of capacitance on the second element in the array. The same experiments are repeated for both arrays having 10% and 20% pre-stretch, and the results are reported as solid green lines in figures 12 and 13, respectively. Here, it can be noted that the first DE undergoes a larger change in capacitance than the second one for both pre-stretch values, even though their initial sizes are identical. In addition, the higher the pre-stretch, the bigger the capacitance change, in agreement with what expected from (7).

The simulated capacitance deviations are reported in the same plots as dotted grey lines in figures 12 and 13. The model succeeds in predicting the overall capacitive trends with satisfactory accuracy. A residual error still exists, mostly visible in the extra-diagonal plots, as well as in the bottom-right one (reasonably due to manufacturing inaccuracies and experimental misalignments). Since the capacitance solely depends on the membrane kinematics (cf (7)), and since the capacitive experiments are performed in displacement-control mode, it was not possible to improve the model accuracy by simply re-tuning the Yeoh parameters. A potential way to explain this deviation is due to the presence of unmodeled phenomena. By considering the characteristics of the experimental setup, it can be assumed that such effects could be caused by a horizontal slipping of the membrane, occurring while the motor is deforming it. In practical experiments, this effect may be

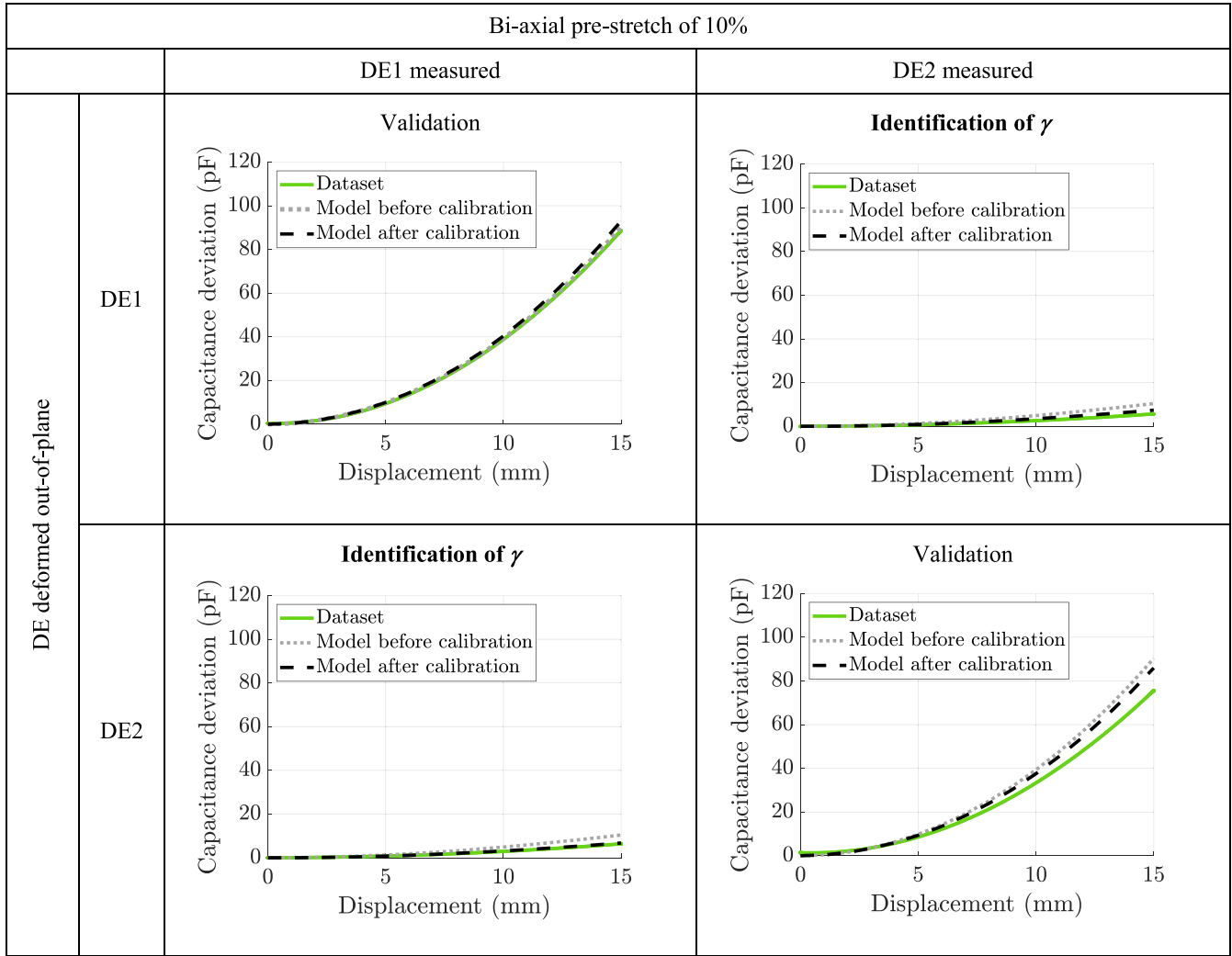


Figure 12. Simulated capacitance deviation before and after boundary condition calibration (depicted in grey and black, respectively), compared with experimental results (depicted with shades of green depending on the applied pre-stretch), for array pre-stretched by 10%. The table reports info on which DE is deformed out-of-plane (row), and which one is subject to capacitance measurements (column). The experiments used for calibration of γ are explicitly denoted with a bold title, while the remaining plots depict model validation.

due to non-perfectly tight clamping at the membrane edges. As a means to further improve the model accuracy, we tried to account for this effect by introducing a correction factor in the boundary condition for the prescribed displacements u in (8):

$$\begin{cases} u = (\lambda_p - 1)X\gamma(d_k) \\ v = (\lambda_p - 1)Y \\ w = 0 \end{cases}, (X, Y, Z)^T \in \Gamma. \quad (11)$$

This way, the pre-stretch along the X -axis (i.e. the longer side of the array, which is possibly most affected by slipping effects) is not kept constant at the original value, but is progressively reduced by a factor γ which depends on the displacement value d_k described in (11). Function γ is calibrated based on only two experiments for the array with 10% pre-stretch, i.e. the extra-diagonal plots in figure 12. The resulting expression for γ is shown in figure 14.

The results obtained with this model modification are reported as dashed black lines in figures 12 and 13, and

show how the implemented mechanism succeed in increasing the accuracy of the capacitance prediction for all the tests (not only for the calibration ones). The improvement due to \mathbf{g} can be especially noticed in the cross-diagonal plots, for which the model calibrated at the 10% pre-stretch provides an accurate extrapolation to the 20% case as well. It is also observed how the newly identified variable boundary condition does not significantly affect the force-deformation curves (results are omitted for conciseness), thus (11) can be implemented without requiring re-calibration of the Yeoh model. We conclude, therefore, that determining whether or not to include \mathbf{g} solely depends on the required accuracy for the capacitive behavior, while it has no meaningful impact on the elastic parameters identification process.

A further validation is performed by comparing the force-displacement curves obtained for different configurations. The results are shown in figures 15 and 16 for the arrays having 10% and 20% pre-stretch, respectively. Each plot depicts the corresponding system configuration, clarifying which DEs

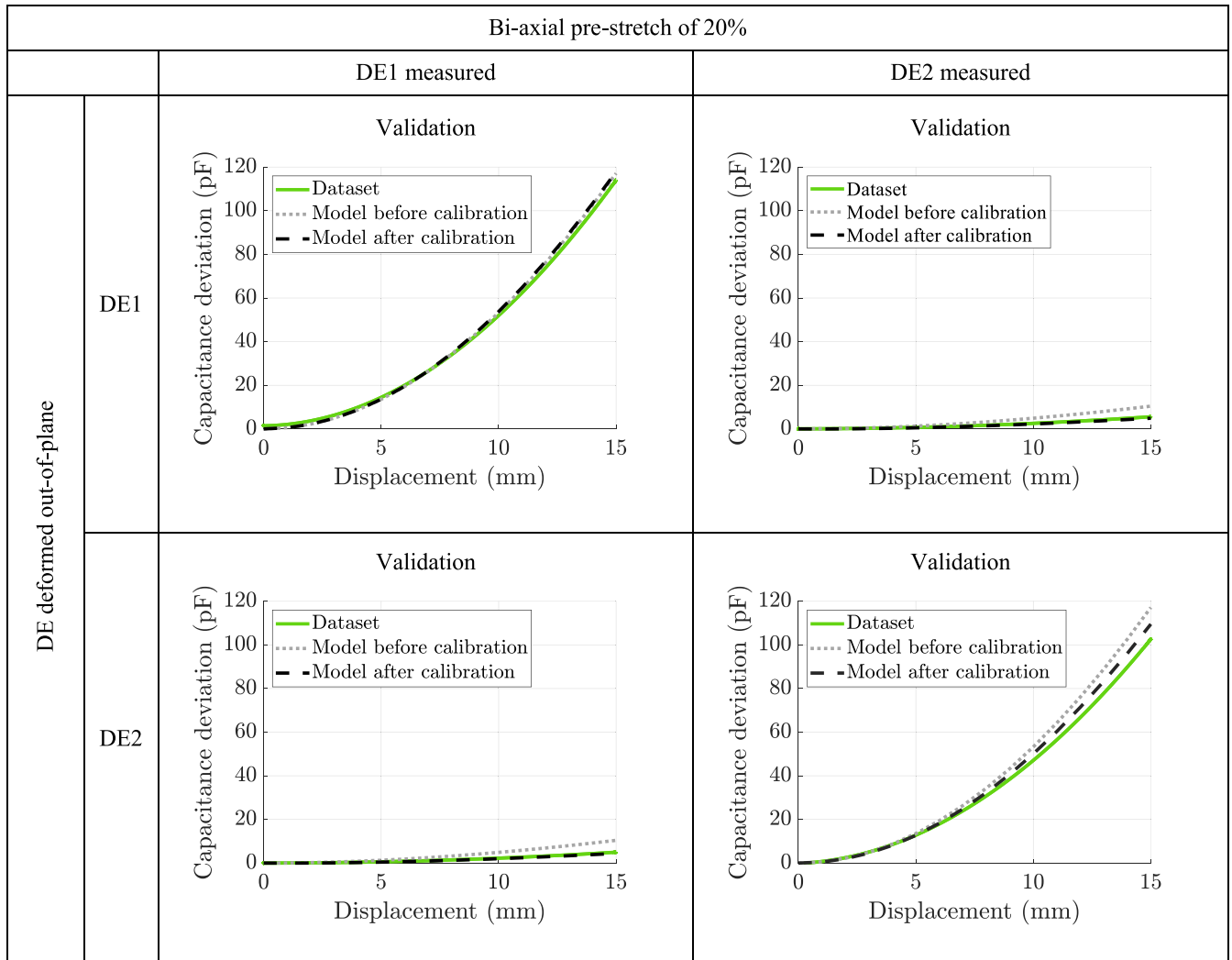


Figure 13. Simulated capacitance deviation before and after boundary condition calibration (depicted in grey and black, respectively), compared with experimental results (depicted with shades of green depending on the applied pre-stretch), for array pre-stretched by 20%. The table reports info on which DE is deformed out-of-plane (row), and which one is subject to capacitance measurements (column). All plots depict model validations.

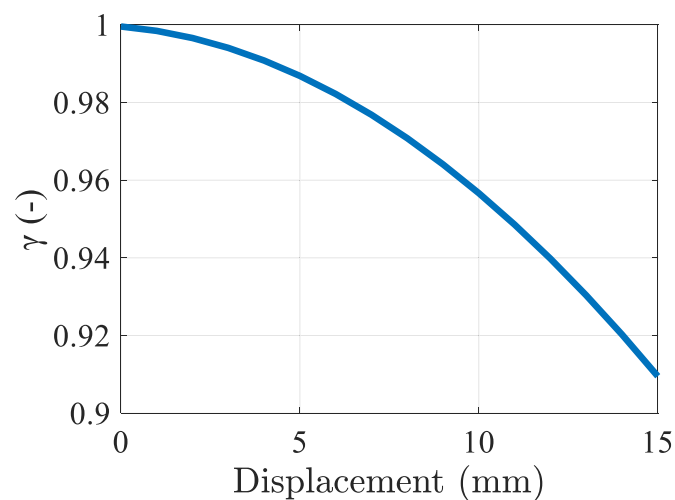


Figure 14. Scaling function γ for the modified boundary condition, used to model the effects of slipping due to non-perfect clamping.

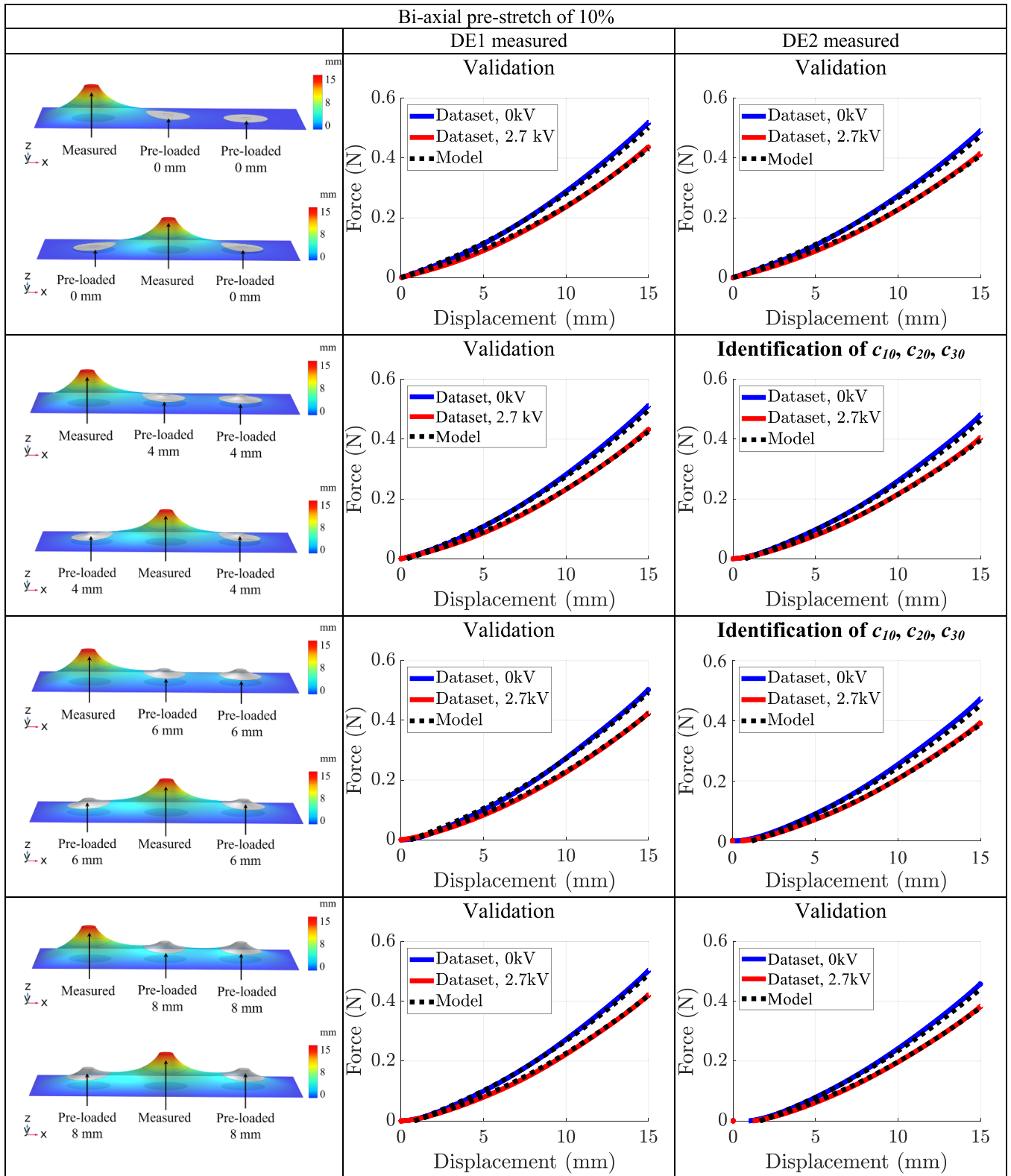


Figure 15. System configuration simulated with the FE model (left column), and corresponding force-displacement characteristics of the first (center column) and second (right column) DEs, by considering different amounts of pre-deflections applied to the neighbors (different rows) for the 10% pre-stretched DE array. Experiments are reported as solid blue (LV) and red (HV) lines, while model predictions as black dashed lines. The experiments used for calibration of the Yeoh parameters are explicitly denoted with a bold title, while the remaining plots depict model validation.

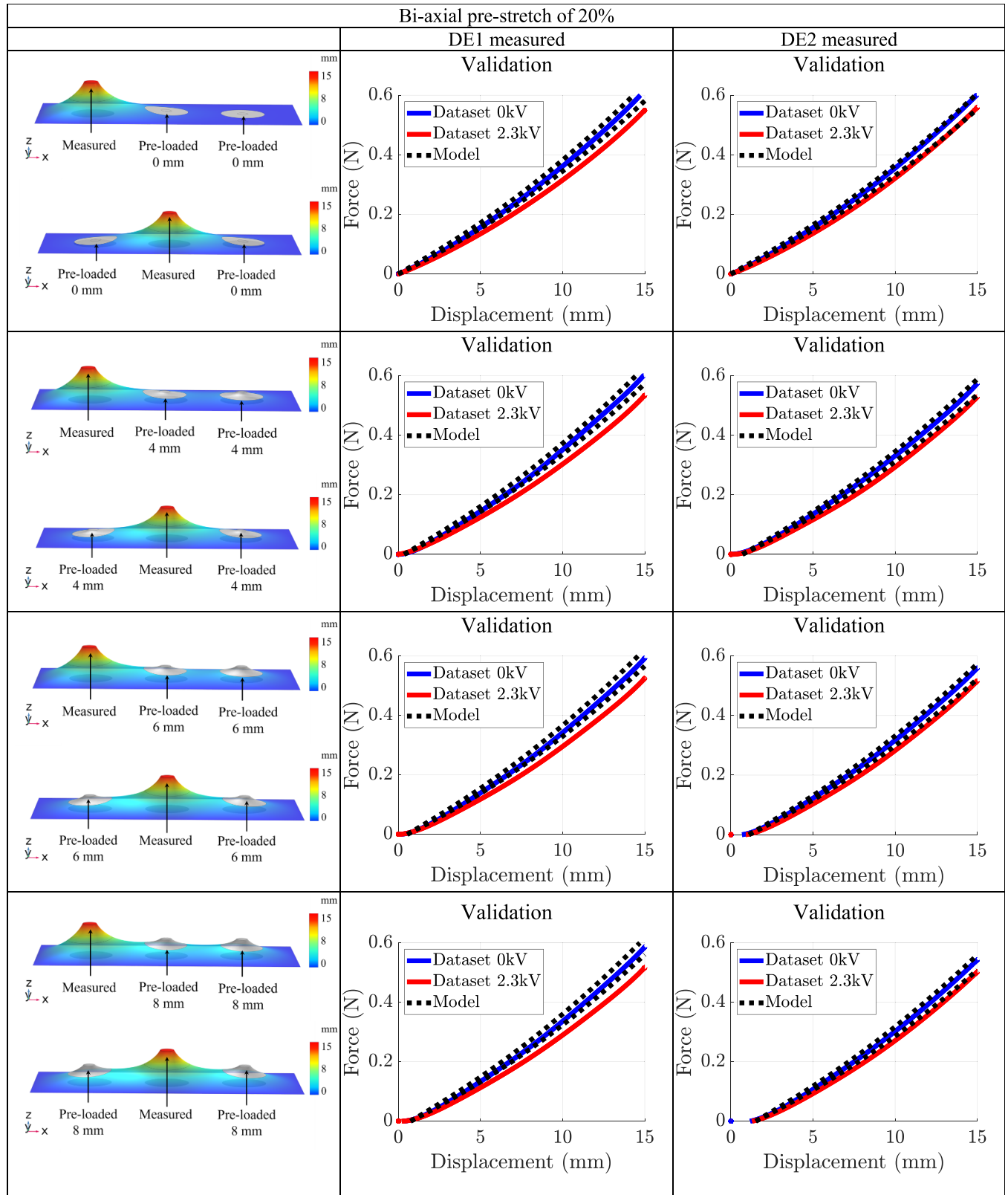


Figure 16. System configuration simulated with the FE model (left column), and corresponding force-displacement characteristics of the first (center column) and second (right column) DEs, by considering different amounts of pre-deflections applied to the neighbors (different rows) for the 20% pre-stretched DE array. Experiments are reported as solid blue (LV) and red (HV) lines, while model predictions as black dashed lines. All plots depict model validations.

Table 2. *FIT* values for the capacitance curves.

Capacitance measured	Pre-stretch 10%		Pre-stretch 20%	
	DE1	DE2	DE1	DE2
DE1 is deformed	86.83%	98.80%	84.05%	99.22%
DE2 is deformed	99.03%	86.39%	99.31%	85.45%
Total average <i>FIT</i>	>92%			

Table 3. *FIT* values for the force-displacement curves.

Force measured	Pre-stretch 10%		Pre-stretch 20%	
	DE1	DE2	DE1	DE2
Pre-load 0 mm	95.65%	96.85%	89.11%	94.84%
Pre-load 4 mm	97.09%	98.04%	86.21%	92.79%
Pre-load 6 mm	94.24%	97.13%	86.55%	91.23%
Pre-load 8 mm	94.44%	95.87%	87.33%	91.50%
Total average <i>FIT</i>	>93%			

are deflected and which one is measured (left column), and the corresponding DE force-displacement curves for the first (center column) and second (right column) DE. Experimental results are reported as solid blue and red lines for the LV and HV cases, respectively, while model predictions are shown as dashed black lines. Two of the plots in figure 15 correspond to those experiments previously used to calibrate the Yeoh model (marked with a bold title), while the remaining ones are used for model validation (about 87% of the total data). An overall satisfactory accuracy is obtained even in this case, with the model showing a good ability to extrapolate for different neighbor pre-deflections and pre-stretch values. In particular, the model well predicts the small, yet observable reduction in force occurring as the neighbors pre-deflection is increased, clearly visible in the experiments. A numerical quantification of the model accuracy is reported in tables 2 and 3, which report the corresponding *FIT* for the capacitance and force experiments (considering the boundary condition (11)). The *FIT* between a measured signal x and its corresponding model prediction x_m is computed as

$$FIT = 100 \left(1 - \frac{\|x - x_m\|}{\|x - \text{mean}(x)\|} \right). \quad (12)$$

The closer *FIT* to 100, the better x_m approximates x . The computed *FIT* quantitatively confirms the high accuracy of the model, with average values larger than 92% for the capacitance and 93% for the force, respectively. Small inaccuracies are observed in some cases (e.g. force data with 20% pre-stretch), reasonably due to manufacturing tolerances. Nevertheless, the obtained results qualify our model as an accurate tool to predict spatially coupled effects in DE arrays.

6. Parameter study

In the following, the FE model validated in section 5 is used to perform a parameter study on the array. Our main goal here is

to gain a general understanding how one can affect the coupling among neighbor DEs by acting on the free design parameters. These results will play an essential role in developing design scaling rules, which in turn will assist future studies targeted at optimizing the array design.

6.1. Tests definition

To study the dependency of the array coupling effects on the free parameters, a FE simulation study is conducted, based on the previously model validated. The aim of the simulations is to evaluate a number of performance indexes, which quantify the amount of coupling for the currently investigated configuration. For the purpose of this study, three different coupling indexes are considered, which are computed as follows:

- *Low voltage force coupling among neighbor DEs*—To compute the first index, we perform a simulation study in which we deflect the central DE out-of-plane up to 0.75D, and evaluate its force-displacement curve in two distinct conditions, i.e. when its two neighbors are not deflected (figure 17(a)) and when they are pre-deflected by a constant amount of 0.4D (figure 17(b)). Both simulations are performed under LV conditions, i.e. $V = 0$ V. A pair of curves like blue ones shown in figure 17(c) are obtained, with the solid line hereby called default configuration (neighbors undeflected) and the dashed line called perturbed configuration (neighbors deflected by 0.4D). The LV force coupling among nearby DEs is quantified by means of the following index

$$\eta_{F,LV} = 100 \frac{\Delta F_{\max,LV}}{F_{\max,LV,\text{default}}}, \quad (13)$$

where $\Delta F_{\max,LV}$ denotes the difference between the maximum values of the two force curves, while $F_{\max,LV,\text{default}}$ represents the maximum force value of the default curve, see figure 17(c). The smaller $\eta_{F,LV}$, the less the force of the second DE depends on the deflection of its neighbors in a relative (%) sense;

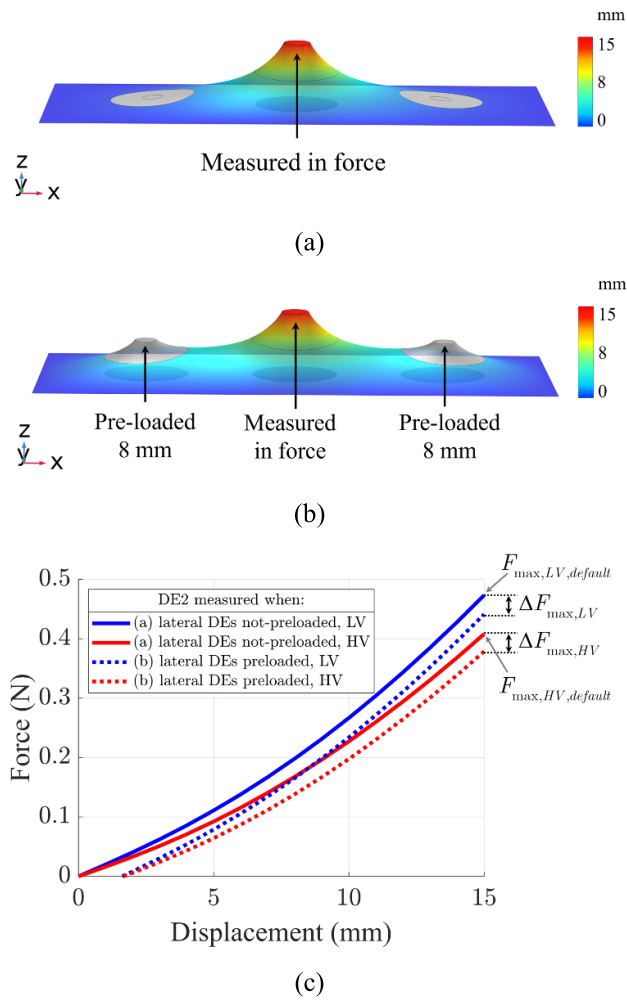


Figure 17. Simulation tests conducted for evaluating the force coupling, (a) lateral DEs not-preloaded and (b) first and third DE deformed out of plane by $0.4D$; (c) resulting force-displacement curves of the second DE in both configurations and relevant parameters for performance evaluation. The plots are obtained by considering nominal values for all parameters.

- *High voltage force coupling among neighbor DEs*—this parameter is obtained similarly to the previous one, but with the difference that this time the characterized DE (i.e. the second one) is subjected to a non-zero constant HV value. In particular, the amount of applied voltage is computed in such a way that the electric field in the initial flat configuration always equal $E_C = 80 \text{ kV mm}^{-1}$. The amount of applied voltage is computed as a function of E_C as follows

$$V = \frac{E_C t_0}{\lambda_p^2}. \quad (14)$$

Note that (14) explicitly depends on both the dielectric initial thickness t_0 and pre-stretch λ_p , therefore changing those parameters will modify the applied voltage accordingly. In this case, curves such as the red ones in figure 17(c) are obtained, with the continuous and dashed lines corresponding again to the default and perturbed configurations. To

quantify the HV force coupling among nearby DEs, the following relative index is considered

$$\eta_{F,HV} = 100 \frac{\Delta F_{\max,HV}}{F_{\max,HV,\text{default}}}, \quad (15)$$

with $\Delta F_{\max,HV}$ denoting the difference between the maximum values of the two high-voltage force curves, and $F_{\max,HV,\text{default}}$ representing the maximum force value of the default HV curve, see figure 17(c). Also in this case, a smaller $\eta_{F,HV}$ implies a weaker coupling among neighbor DEs;

- *Capacitance coupling among neighbor DEs*—to quantify the capacitance coupling, two different simulations are considered, in which we deflect out-of-plane the second and the first DE respectively, up to a maximum displacement of $0.75D$. In both cases, we acquire the increment in capacitance (with respect to the default configuration) of the second DE (cf figures 18(a) and (b)). To quantify the capacitance coupling among DEs, we use the index

$$\eta_C = 100 \frac{\Delta C_{\max,\text{perturbed}}}{\Delta C_{\max,\text{default}}}, \quad (16)$$

in which $\Delta C_{\max,\text{default}}$ and $\Delta C_{\max,\text{perturbed}}$ are the maximum values of capacitance increment when the second and first DE are deformed, respectively. The bigger η_C , the bigger the changes in capacitance due to self-deformation of the DE relatively to the changes in capacitance due to displacements of its neighbors (in %).

Simulation studies are performed under the above conditions, in order to compute coupling coefficients (13), (15), and (16) for a number of distinct array configurations. All simulation studies are conducted by considering all the array parameters equal to their nominal values, except for a specified one (or a specified subset), which is (are) changed appropriately for the given study. The nominal values of the geometric and material parameters are chosen as in table 1, while the nominal bi-axial pre-stretch is set to $\lambda_p = 1.10$.

In the above analyses, the measured DE unit, used for the evaluation of the coupling factors, is the second one (i.e. the central one) of the array. Because this unit is located in between a couple of neighbor units, it is expected that even in the case on larger arrays (with more three units), internal units would show responses (in terms of the coupling parameters) similar to those discussed in the following.

Based on practical design considerations, the following parameter studies are chosen for the subsequent investigation:

- *Electrode spacing*—for the first investigation, we consider the electrode spacing d ranging from 1 mm to 11 mm, with increments of 2.5 mm. The minimum spacing value is chosen based on considerations on air dielectric strength (i.e. 3 kV mm^{-1} [55]). Reducing the spacing between DEs allows increasing the actuation density of the system given the same total array area, but it is also expected to increase the amount of coupling among neighbors;

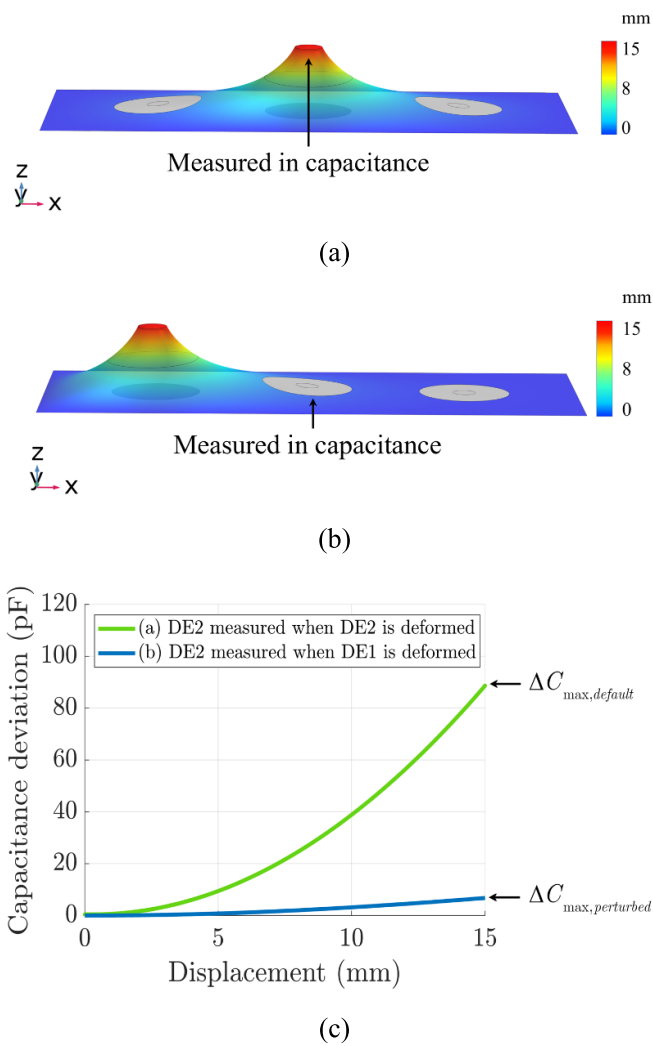


Figure 18. Simulation test conducted for evaluating the capacitance coupling, (a) undeformed configuration and (b) deformed configuration of first DE (c) resulting capacitance deviation-displacement curves of the second DE in both configurations and relevant parameters for performance evaluation. The plots are obtained by considering nominal values for all parameters.

- *Distance between electrodes and outer edges*—for the second investigation, we consider the distance between electrodes and outer edges b ranging from 10 mm to 50 mm, with increments of 5 mm. This study will allow us to understand the impact of boundary effects on the array coupling behavior;
- *Membrane bi-axial pre-stretch*—for the third investigation, we consider a bi-axial pre-stretch λ_p applied to both λ_1 and λ_2 ranging from 1.10 to 1.80, with increments of 0.05. The study of this parameter will allow us to understand if we can affect the amount of coupling by also pre-stretching more the membrane (thus making it stiffer) during the array manufacturing process;
- *Area scaling factor*—for the fourth investigation, we consider a down-scaling of all the membrane geometric parameters except the thickness (i.e. L , H , D , d , and b) by the same factor (ranging from 1 to 100). This analysis is of practical interest in view of a down-scaling of the DE array;

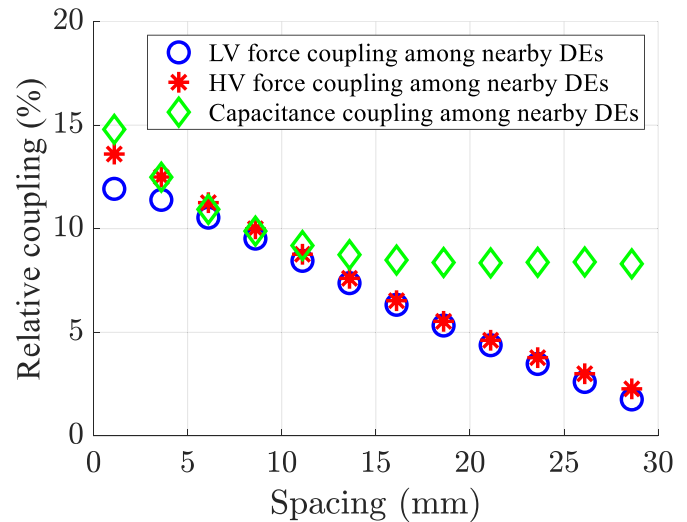


Figure 19. Results of parameter study, electrode spacing.

- *Electrode shape*—for the fifth and final study, a dedicated investigation is conducted to understand whether the shape of the electrode has any impact of the performance of the array, or if only its area represents a relevant design parameter.

6.2. Parameter study results

Simulation studies are conducted according to the modalities described in section 6.1. The results of the first four parameters (i.e. electrode spacing, distance from the edge, pre-stretch, area scaling) are shown in figures 19–22, where each plot reports three different coupling indexes $\eta_{F, LV}$ (blue circles), $\eta_{F, HV}$ (red stars), and η_C (green diamonds), computed for different values of the parameter under investigation. For the fifth parameter (electrode geometry), the results are shown in figure 23 in terms of actual force and capacitive curves only, for a better visualization. A more detailed analysis of the results is reported in the following.

The first results, reported in figure 19, show the effects of the electrode spacing. It can be observed that the closer the DEs are, the more pronounced the coupling effect is, both in terms of force and capacitance measurements. This behavior is somehow expected, since the closer the membranes the higher the mutual interference of their corresponding stress fields. The two values of force couplings are on the order of 12% for the minimum spacing of 1 mm (minimum spacing which avoids breakdown through air when adjacent electrodes are at different potentials), and decrease progressively until they reach a value of 1% for the maximum spacing value of 15 mm, i.e. 75% of the DEs diameter. Although the two force coupling parameters are overall similar, the HV one is always slightly higher than the LV, confirming that DE stiffness is less affected by the spatial coupling than the actuation force. Interestingly, the capacitance coupling shows a different trend. While showing similar values to the force coupling in case of minimum spacing (about 15%), it converges to a 8% plateau for increasing spacing. This effect can be explained as follows.

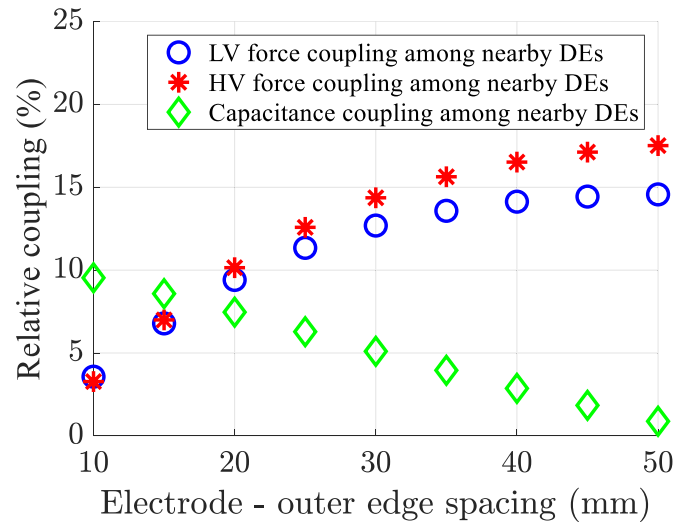


Figure 20. Results of parameter study, distance between electrodes and outer edges.

Even though the DEs are located far apart from each other, and thus their forces are overall independent, the overall membrane still undergoes significant global deformations even when only one of the DEs is deformed. This result appears to be particularly interesting for the future application of the array in distributed sensing applications.

Next, the boundary effects are investigated in figure 20, in which simulation studies are conducted for different distances between electrodes and passive edges of the membranes, where the boundary conditions are applied. As it can be noted, the force coupling values increase for higher distances between DEs and outer edges. Also in this case, the coupling increases more for the HV case, rather than the LV one. This is due to the larger surface relaxation of the array, as the clamping effect of the outer edge is attenuated by the higher spacing value. Conversely, increasing the distance between DEs and the outer edges results in a lower capacitance coupling, which converges from an initial 10% to almost 0%. Therefore, combining this result with the previous one, we can determine that the residual capacitance coupling observed in figure 19 for widely-spaced DEs was mostly due to boundary effects, rather than the deformation of the neighbor units. By properly playing with this parameter, one can tune the amount of capacitive coupling in the array, making the sensing properties of the different membranes more or less interdependent.

Figure 21 shows the results for different amounts of bi-axial pre-stretch applied to the membrane. As the pre-stretch increases, the array thickness decreases accordingly, resulting in an increase in capacitance (cf (7)). However, since the pre-stretch also increases the membrane stiffness, it suppresses the influence of the deformed DE membrane on the capacitance variation of the measured one, thus reducing the capacitance coupling to a value of approximately 2%. Conversely, the force coupling trends remain somehow unchanged at about 8% for increasing pre-stretch values above 25%. These results highlight how the pre-stretch represents an effective

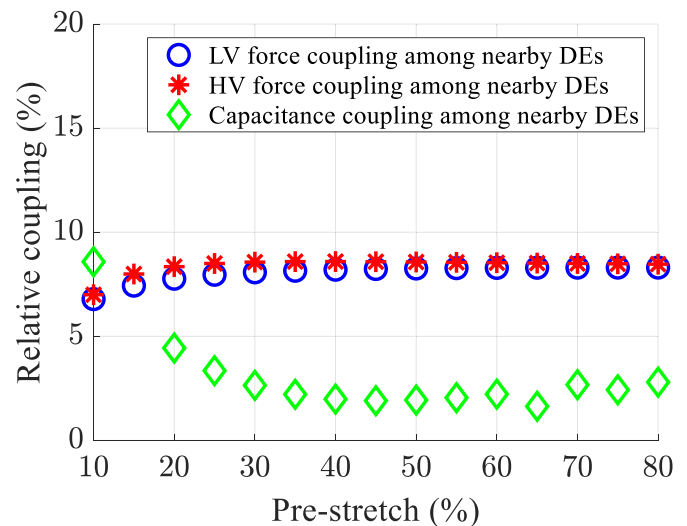


Figure 21. Results of parameter study, membrane bi-axial pre-stretch.

tuning parameter when one wants to reduce the sensing coupling without significantly suppressing the force and actuation ones.

Figure 22 shows the results of the study in which the overall array surface is downscaled, while keeping the membrane thickness and pre-stretch constant. This study represents a scenario in which miniaturization of the DE array is sought. As can be seen, as the scaling varies, all the three coupling factors remain unchanged. This result is expected and consistent with the assumptions of a membrane model, according to which the capacitance and force scale with the area and the down-scaling factor, respectively. Such a result confirms that the spatial coupling effects are practically invariant to the scale of the given application, and represents a key aspect for future cooperative micro-actuator applications.

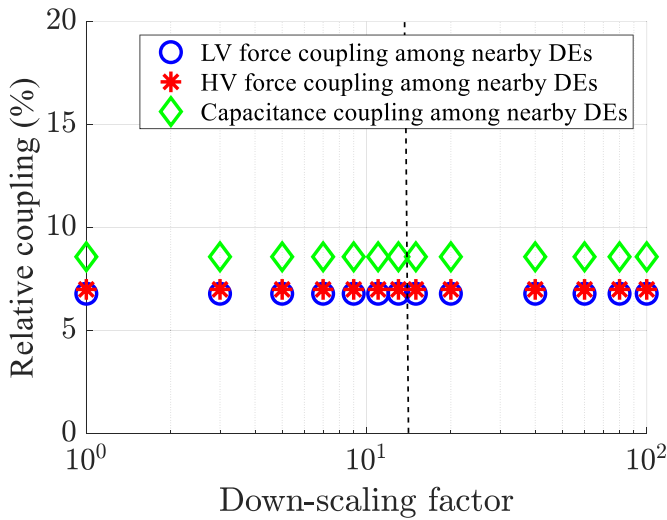


Figure 22. Results of parameter study, area down-scaling factor. The black dotted line highlights the scaling factor value over which the electrode spacing d becomes smaller than the minimum value allowed to avoid breakdown through air.

In practice, we expect this outcome to hold true as long as the membrane assumption remains valid for the DE, i.e. the overall surface dimensions are much larger than the thickness of the membrane ($t_0 = 50 \mu\text{m}$ in this specific study). In the case of highly miniaturized applications (in the mm and sub-mm scale), modifications to the model might be required, as some of the assumptions underlying elastic membranes' theory would no longer hold true. Nevertheless, the detailed investigation of those effects falls beyond the scope of this paper. As an additional remark, we point out that those simulations were conducted by keeping the same pre-stretch and thickness, thus resulting in the same amount of voltage according to (14). Reducing the scale by a factor higher than a certain threshold (here, approximately 13), the electrode spacing d becomes smaller than the minimum value allowed by electrical breakdown through air (1.1 mm for this particular case). This critical value is marked with a black dotted line in figure 22. When developing real applications, this factor must be appropriately taken into account, e.g. by using thinner DE membranes (so as to reduce the applied voltage) or using further low-stiffness insulation layers on top of the array.

Finally, we perform a further study to investigate the effects of the shape of the electrode. In particular, we are interested in understanding if the actuation and sensing performance of the array depends on the particular shape of the electrodes, or rather on its area only. To this end, we perform an additional comparative study in which we consider two electrodes having the same active areas but different shapes, namely a circle (as in the nominal case) and a square, see figure 23(a). For the sake of clarity, this study is performed by simply showing the effects of the electrode shape on the resulting force-displacement and capacitance curve of the second DE, while it undergoes an out-of-plane deformation. Therefore, no analysis of the coupling indexes is presented in this case. The results, reported in figure 23(b) for the force and in figure 23(c)

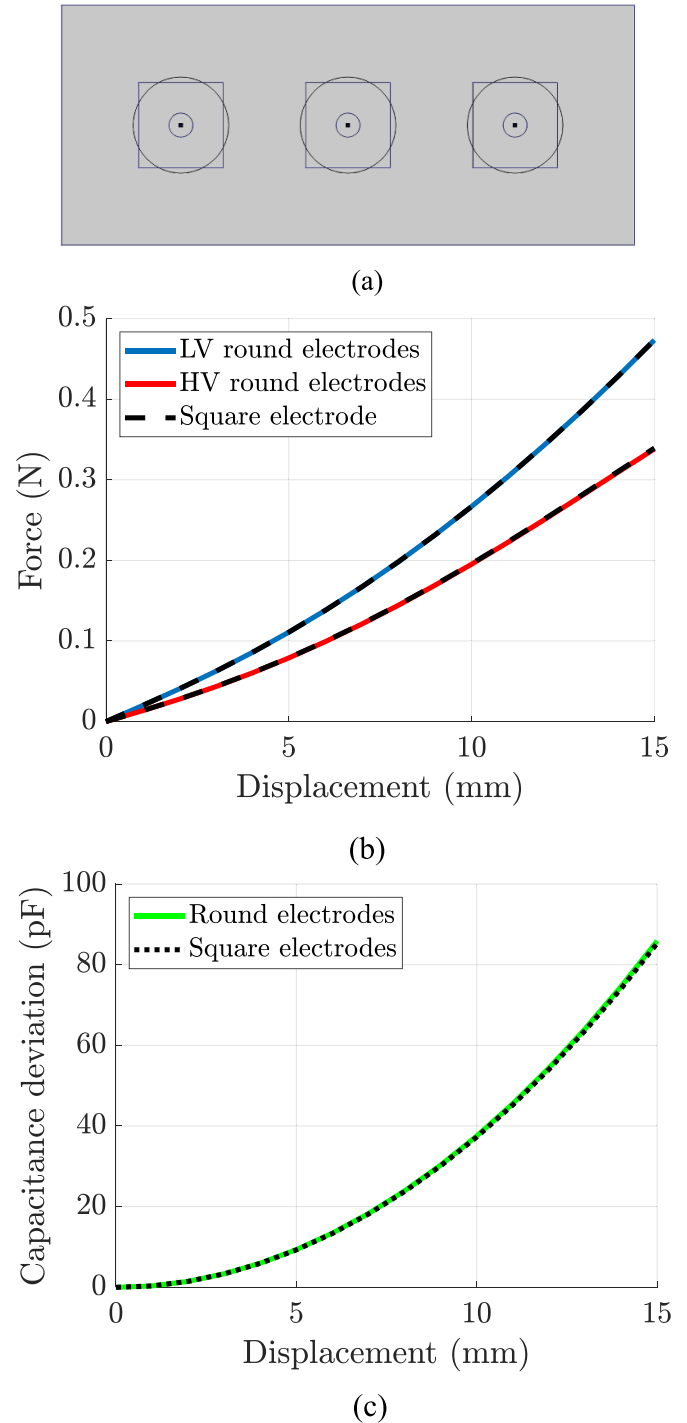


Figure 23. Effects of electrode shape on the resulting array performance. (a) Top view of the array, showing overlapping round and square electrodes; (b) comparison among force-displacement curves obtained with both types of electrode shape; (c) comparison among capacitance deviation curves obtained with both types of electrode shape.

for the capacitance deviation, clearly show that the shape of the electrode has virtually no impact on the resulting array behavior. As a result, we conclude that the electrodes can be shaped in an arbitrary way, and only their areas should be considered as a relevant parameters. For instance, one may

prefer squared electrodes over circular ones, since they would result in a higher amount of active area (i.e. actuation and sensing features) given the same minimum distance among DEs.

7. Conclusions

In this paper we presented a FE study conducted on a 3-by-1 soft array of DEs. The layout considered in this study represents a simple archetypal concept of DE array, based on a fully-polymeric architecture, which potentially lends itself to the development of more complex multi-actuator layouts (e.g. with a larger number of active DE units). A physics-based model of the array was calibrated and validated based on an extensive experimental campaign, in which spatially-coupled electro-mechanical effects have been investigated under several array configurations and parameters. The model allowed us to reproduce the behavior of the DEs force and capacitance responses for different types of electro-mechanical loading conditions, and by considering different combinations of deflected neighbors. Average fit values on the order of 93% and 92% were obtained for the force and capacitance responses, respectively. The calibrated model also allowed us to understand the role of some design parameters on the cooperative performance of the array, quantified in terms of the variations of the force and capacitance of a DE element due to the deformation of the neighbor elements (force and capacitance coupling). The following main findings were obtained, which will be used as reference rules for the design of future cooperative DE applications:

- Increasing the spacing among DEs reduces their force coupling while keeping the capacitance coupling constant (provided that a certain threshold is exceeded);
- Increasing the distance between DEs and outer edges increases the force coupling and decreases at the same time the capacitive one;
- Increasing the pre-stretch has virtually no impact on the force coupling, while it reduces the capacitive coupling;
- All the coupling effects remain unchanged when scaling the array surface area geometry while keeping the film thickness unchanged, provided that the resulting array still satisfies a membrane assumption (large surface-to-thickness ratio);
- Only the surface area of the electrodes, and not their specific shapes, has an impact on the resulting array actuation and sensing performance.

In future studies, the obtained findings will be used to perform design optimization studies, aimed at designing cooperative DE actuator/sensor systems with desired performance. In particular, further extensions of the model will be conducted, to explore feasibility of the concept in a more accurate way i.e.: numerically efficient routines for optimizing the design of the biasing elements for the full cooperative DEA array; additional dynamic studies with a consequent inclusion of hysteretic, inertial, and thermal effects in the model, to improve its prediction capabilities in a wider set of operating conditions and loading scenarios; investigation of more complex

array layouts, featuring a larger number of units or complex matrix arrangements.

Data availability statement

All data that support the findings of this study are included within the article (and any supplementary files).

Acknowledgments

The authors gratefully acknowledge the support of the Deutsche Forschungsgemeinschaft (DFG, German Research Foundation) through Priority Program SPP 2206 ‘Cooperative Multistage Multistable Microactuator Systems’ (Projects: RI3030/2-1, SCHU1609/7-1, SE704/9-1), and the European Union’s Horizon 2020 research and innovation programme under the Marie Skłodowska-Curie grant agreement No 893674 (DEtune).

ORCID iDs

Sipontina Croce  <https://orcid.org/0000-0002-9324-6848>
 Julian Neu  <https://orcid.org/0000-0002-0719-9011>
 Giacomo Moretti  <https://orcid.org/0000-0003-1606-7392>
 Jonas Hubertus  <https://orcid.org/0000-0001-9388-0454>
 Gianluca Rizzello  <https://orcid.org/0000-0002-7017-698X>

References

- [1] Schleer P, Vossel M, Heckmann L, Drobinsky S, Theisgen L, de la Fuente M and Radermacher K 2021 Usability of cooperative surgical telemanipulation for bone milling tasks *Int. J. Comput. Assist. Radiol. Surg.* **16** 311–22
- [2] Mohammadi M, Franchi A, Barcelli D and Prattichizzo D 2016 Cooperative aerial tele-manipulation with haptic feedback *IEEE Int. Conf. Intell. Robot. Syst.* **2016** 5092–8
- [3] Musić S, Salvietti G, Dohmann P B, Chinello F, Prattichizzo D and Hirche S 2019 Human-robot team interaction through wearable haptics for cooperative manipulation *IEEE Trans. Haptics* **12** 350–62
- [4] Tuci E, Alkilabi M H M and Akanyeti O 2018 Cooperative object transport in multi-robot systems: a review of the state-of-the-art *Front. Robot. AI* **5** 59
- [5] Rugthum T and Tao G 2016 An adaptive actuator failure compensation scheme for a cooperative manipulator system *Robotica* **34** 1529–52
- [6] Feddema J T, Lewis C and Schoenwald D A 2002 Decentralized control of cooperative robotic vehicles: theory and application *IEEE Trans. Robot. Autom.* **18** 852–64
- [7] Ataka M, Fujita H, Omodaka A and Takeshima N 1993 Fabrication and operation of polyimide bimorph actuators for a ciliary motion system *J. Microelectromech. Syst.* **2** 146–50
- [8] Fukuta Y, Chapuis Y-A, Mita Y and Fujita H 2006 Design, fabrication, and control of MEMS-based actuator arrays for air-flow distributed micromanipulation *J. Microelectromech. Syst.* **15** 912–26
- [9] Bohringer K F, Donald B R and MacDonald N C 1996 Single-crystal silicon actuator arrays for micro

- manipulation tasks *Proc. IEEE Micro Electro Mechanical Systems (MEMS)* pp 7–12
- [10] Habibi A, Dedu E, Bourgeois J, Laurent G J and Le Fort-Piat N 2014 Distributed Pneumatic MEMS for Fast Conveyance of Fragile Objects
- [11] Carpi F, Frediani G, Gerboni C, Gemignani J and De Rossi D 2014 Enabling variable-stiffness hand rehabilitation orthoses with dielectric elastomer transducers *Med. Eng. Phys.* **36** 205–11
- [12] Pelrine R E, Kornbluh R D and Joseph J P 1998 Electrostriction of polymer dielectrics with compliant electrodes as a means of actuation *Sens. Actuators A* **64** 77–85
- [13] Suo Z 2010 Theory of dielectric elastomers *Acta Mech. Solida Sin.* **23** 549–78
- [14] Carpi F, De Rossi D, Kornbluh R, Pelrine R and Sommer-Larsen P 2008 *Dielectric Elastomers as Electromechanical Transducers: Fundamentals, Materials, Devices, Models and Applications of an Emerging Electroactive Polymer Technology* (Amsterdam: Elsevier)
- [15] Huu Chuc N et al 2008 A dielectric elastomer actuator with self-sensing capability *Proc. SPIE* **6927** 69270V
- [16] Rizzello G, Naso D, York A and Seelecke S 2016 Closed loop control of dielectric elastomer actuators based on self-sensing displacement feedback *Smart Mater. Struct.* **25** 035034
- [17] Wang S, Kaaya T and Chen Z 2020 Self-sensing of dielectric elastomer tubular actuator with feedback control validation *Smart Mater. Struct.* **29** 075037
- [18] Kornbluh R 2016 High-speed electrically actuated elastomers with strain greater than 100% *Science* **287** 836–40
- [19] McCoul D and Pei Q 2015 Tubular dielectric elastomer actuator for active fluidic control *Smart Mater. Struct.* **24** 105016
- [20] Boys H, Frediani G, Poslad S, Busfield J and Carpi F 2017 A dielectric elastomer actuator-based tactile display for multiple fingertip interaction with virtual soft bodies SPIE, Electroactive Polymer Actuators and Devices (EAPAD) United States **10163** 101632D
- [21] Qu X et al 2021 Refreshable Braille display system based on triboelectric nanogenerator and dielectric elastomer *Adv. Funct. Mater.* **31** 2006612
- [22] Giousouf M and Kovacs G 2013 Dielectric elastomer actuators used for pneumatic valve technology *Smart Mater. Struct.* **22** 104010
- [23] Hosoya N, Masuda H and Maeda S 2019 Balloon dielectric elastomer actuator speaker *Appl. Acoust.* **148** 238–45
- [24] Garnell E 2020 Dielectric elastomer loudspeakers: models, experiments and optimization p 196
- [25] Moretti G, Rizzello G, Fontana M and Seelecke S 2021 A multi-domain dynamical model for cone-shaped dielectric elastomer loudspeakers SPIE Smart Structures + Nondestructive Evaluation **11587** 53
- [26] Mao G, Wu L, Fu Y, Chen Z, Natani S, Gou Z, Ruan X and Qu S 2018 Design and characterization of a soft dielectric elastomer peristaltic pump driven by electromechanical load *IEEE/ASME Trans. Mechatron.* **23** 2132–43
- [27] Qiu Y, Zhang E, Plamthottam R and Pei Q 2019 Dielectric elastomer artificial muscle: materials innovations and device explorations *Acc. Chem. Res.* **52** 316–25
- [28] Almanza M, Clavica F, Chavanne J, Moser D, Obrist D, Carrel T, Civet Y and Perriard Y 2021 Feasibility of a dielectric elastomer augmented aorta *Adv. Sci.* **8** 1–13
- [29] Huang B, Li M, Mei T, McCoul D, Qin S, Zhao Z and Zhao J 2017 Wearable stretch sensors for motion measurement of the wrist joint based on dielectric elastomers *Sensors* **17** 2708
- [30] Böse H, Ocak D and Ehrlich J 2016 Applications of pressure-sensitive dielectric elastomer sensors *Electroact. Polym. Actuators Devices* **9798** 97982C
- [31] Matysek M, Lotz P, Winterstein T and Schlaak H F 2009 Dielectric elastomer actuators for tactile displays *World Haptics 2009—Third Joint EuroHaptics Conf. and Symp. on Haptic Interfaces for Virtual Environment and Teleoperator Systems (March)* pp 290–5
- [32] Zhao H, Hussain A M, Israr A, Vogt D M, Duduta M, Clarke D R and Wood R J 2020 A wearable soft haptic communicator based on dielectric elastomer actuators *Soft Robot.* **7** 451–61
- [33] Edouard L, Shea H and Gao M 2021 Hydraulically amplified dielectric actuator taxels *US2021/031646A1*
- [34] Qu S and Suo Z 2012 A finite element method for dielectric elastomer transducers *Acta Mech. Solida Sin.* **25** 459–66
- [35] Schlögl T and Leyendecker S 2016 Electrostatic–viscoelastic finite element model of dielectric actuators *Comput. Methods Appl. Mech. Eng.* **299** 421–39
- [36] Simone F, Linnebach P, Rizzello G and Seelecke S 2018 A finite element model of rigid body structures actuated by dielectric elastomer actuators *Smart Mater. Struct.* **27** 065001
- [37] Garcia L A and Trindade M A 2019 Finite element modeling and parametric analysis of a dielectric elastomer thin-walled cylindrical actuator *J. Braz. Soc. Mech. Sci. Eng.* **41** 1–9
- [38] Moretti G, Rizzello G, Fontana M and Seelecke S 2022 Finite element modelling of the vibro-acoustic response in dielectric elastomer membranes SPIE, Electroactive Polymer Actuators and Devices (EAPAD) XXIV **12042** 60
- [39] Croce S, Neu J, Hubertus J, Seelecke S, Schultes G and Rizzello G 2022 Finite element modeling and parameter study of a fully-polymeric array of coupled dielectric elastomers *Electroactive Polymer Actuators and Devices (EAPAD) XXIV* p 120420B
- [40] Neu J, Croce S, Hubertus J, Schultes G, Seelecke S and Rizzello G 2021 Characterization and modeling of an array of dielectric elastomer taxels SPIE, Electroactive Polymer Actuators and Devices (EAPAD) XXIII vol 11587 p 24
- [41] Croce S, Neu J, Hubertus J, Seelecke S, Schultes G and Rizzello G 2021 Model-based design optimization of soft polymeric domes used as nonlinear biasing systems for dielectric elastomer actuators *Actuators* **10** 209
- [42] Neu J, Croce S, Hubertus J, Schultes G, Seelecke S and Rizzello G 2022 Experimental characterization of the mechanical coupling in a DE-array *Electroactive Polymer Actuators and Devices (EAPAD) XXIV* p 120420H
- [43] Lau G K, La T G, Foong E S W and Shrestha M 2016 Stronger multilayer acrylic dielectric elastomer actuators with silicone gel coatings *Smart Mater. Struct.* **25** 125006
- [44] Rosset S, Ararom O A, Schlatter S and Shea H R 2016 Fabrication process of silicone-based dielectric elastomer actuators *J. Vis. Exp.* **2016** 1–13
- [45] Rosset S and Shea H R 2013 Flexible and stretchable electrodes for dielectric elastomer actuators *Appl. Phys. A* **110** 281–307
- [46] Hubertus J, Neu J, Croce S, Rizzello G, Seelecke S and Schultes G 2021 Nanoscale nickel-based thin films as highly conductive electrodes for dielectric elastomer applications with extremely high stretchability up to 200% *ACS Appl. Mater. Interfaces* **13** 39894–904
- [47] Bruch D, Hau S, Loew P, Rizzello G and Seelecke S 2018 Fast model-based design of large stroke dielectric elastomer membrane actuators biased with pre-stressed buckled beams *Electroactive Polymer Actuators and Devices (EAPAD) XX* vol 10594 pp 62–69
- [48] Loew P, Rizzello G and Seelecke S 2017 Permanent magnets as biasing mechanism for improving the performance of

- circular dielectric elastomer out-of-plane actuators *Proc. SPIE* **10163** 101630Y
- [49] Wacker Chemie A G ELASTOSIL® FILM 2030 250/50
- [50] Holzapfel G A 2002 Nonlinear solid mechanics: a continuum approach for engineering science *Meccanica* **37** 489–90
- [51] Moretti G, Rizzello G, Fontana M and Seelecke S 2022 High-frequency voltage-driven vibrations in dielectric elastomer membranes *Mech. Syst. Signal Process.* **168** 108677
- [52] Dorfmann L and Ogden R W 2014 *Nonlinear Theory of Electroelastic and Magnetoelastic Interactions* vol 9781461495 (New York: Springer) **XI**, 313
- [53] Croce S *et al* Finite element modeling and simulation of a soft array of dielectric elastomer actuators *Proc. ASME 2021 Conf. Smart Mater. Adapt. Struct. Intell. Syst. SMASIS 2021 (October 2021)* (<https://doi.org/10.1115/SMASIS2021-67752>)
- [54] Vertechy R, Frisoli A, Bergamasco M, Carpi F, Frediani G and De Rossi D 2012 Modeling and experimental validation of buckling dielectric elastomer actuators *Smart Mater. Struct.* **21** 094005
- [55] Yu L, Vudayagiri S, Jensen L A and Skov A L 2020 Temperature dependence of dielectric breakdown of silicone-based dielectric elastomers *Int. J. Smart Nano Mater.* **11** 129–46